Monthly Notices of the ROYAL ASTRONOMICAL SOCIETY

MNRAS **549,** 1–23 (2026)
Advance Access publication 2026 April 30

https://doi.org/10.1093/mnras/stag824

JADES Dark Horse: demonstrating high-multiplex observations with *JWST*/NIRSpec dense-shutter spectroscopy in the JADES Origins Field

Francesco D'Eugenio [1,2★] Erica J. Nelson [3] Daniel J. Eisenstein [4] Roberto Maiolino [1,2,5] Stefano Carniani [6] Jan Scholtz [1,2] Mirko Curti [7] Christopher N. A. Willmer [8] Andrew J. Bunker [9] Jakob M. Helton [10] Ignas Juodžbalis [1,2] Fengwu Sun [4] Sandro Tacchella [1,2] Santiago Arribas [11] Alex J. Cameron [9] Stéphane Charlot [12] Emma Curtis-Lake [13] Kevin Hainline [8] Benjamin D. Johnson [4] Brant Robertson [14] Christina C. Williams [15] Chris Willott [16] William M. Baker [17] Jacopo Chevallard [9] A. Lola Danhaive [1,2] Yuki Isobe [1,2] Xihan Ji [1,2] Zhiyuan Ji [8] Gareth C. Jones [1,2] Nimisha Kumari [18] Tobias J. Looser [4] Jianwei Lyu [8] Eleonora Parlanti [6] Michele Perna [11] Dávid Puskás [1,2] Pierluigi Rinaldi [8] Charlotte Simmonds [1,2,19] Yang Sun [8] Hannah Übler [20] Giacomo Venturi [6] Joris Witstok [21,22] Zihao Wu [4] and Yongda Zhu [8]

Affiliations are listed at the end of the paper

Accepted 2026 April 2. Received 2026 March 8; in original form 2025 October 17

ABSTRACT

We present *James Web Space Telescope*/NIRSpec dense-shutter spectroscopy (DSS). This novel observing strategy with the NIRSpec/multi-shutter assembly (MSA) deliberately permits a high number of controlled spectral overlaps to reach extreme multiplex while retaining the low background of slit spectroscopy. In a single configuration over the JADES Origins Field, we opened shutters on all faint ($m_{\rm F444W} < 30$ mag) $z_{\rm phot} > 3$ candidates, prioritizing emission-line science and rejecting only bright continuum sources. Using 33.6 and 35.8 ks on-source in G235M and G395M, we observed a single mask with ∼850 sources, obtaining spectroscopic redshifts for ∼540 galaxies over $2.5 \lesssim z \lesssim 8.9$. The per-configuration target density in DSS mode is 4–5× higher than standard no- and low-overlap MSA strategies (<200 sources), with no loss in redshift precision or accuracy. Line-flux sensitivities are 30 per cent lower at fixed exposure time, matching the expected increase in background noise, but the gain in survey speed is 5× in our setup, more than justifying the penalty. The measured line sensitivity exceeds NIRCam slitless spectroscopy by at least ∼5× (∼25× in exposure time) at $\lambda \sim 4$ μm, demonstrating that DSS is a compelling method to gain deep, wide-band spectra for large samples. Crucially, NIRSpec/MSA could deliver even higher target allocation densities than those used here. We derive H α-based star-formation rates, gas-phase metallicities (including a large sample suitable for strong-line calibrations), and identify rare mini-quenched galaxies and broad-line AGN. DSS is immediately applicable wherever deep imaging enables robust pre-selection and astrometry, providing an efficient method to obtain large samples of faint emission-line galaxies, a compelling middle ground between the completeness of slitless surveys and the sensitivity and bandwidth of NIRSpec/MSA.

Key words: instrumentation: spectrographs – methods: observational – techniques: spectroscopic – surveys – galaxies: high-redshift – galaxies: ISM.

1 INTRODUCTION

With its unprecedented ability to obtain sensitive near-infrared spectroscopy from 1–5 μm, *James Web Space Telescope (JWST*; J. P. Gardner et al. 2023) is providing revolutionary capabilities to trace galaxy evolution to the earliest cosmic times. Spectroscopic redshifts and emission-line fluxes allow us to map the physical conditions within galaxies as they assemble and evolve, providing insights into gas-phase metallicities, ionization states, and instantaneous star formation rates. Further, these observations enable us to dissect the role of active galactic nuclei (AGN) in regulating early galaxy growth and to understand how supermassive black holes themselves grew during the first billion years after the big bang. As such, large spectroscopic surveys of faint early galaxies provide key insights on the early stages of galaxy growth.

★ E-mail: francesco.deugenio@gmail.com

JWST offers two primary approaches for near-infrared (NIR) multi-object spectroscopy: NIRISS or NIRCam slitless grism modes (T. P. Greene et al. 2017; C. J. Willott et al. 2022) and the NIRSpec multi-shutter assembly (MSA; P. Ferruit et al. 2022). However, these approaches present a trade-off that limits survey efficiency. MSA spectroscopy achieves substantially higher sensitivity by masking away most of the background and benefits from a wider instantaneous bandwidth and larger pixels that reduce detector noise. Yet it suffers from low-targeting completeness: The fixed grid of MSA shutters vignette approximately half of all sources just by chance, and the standard practice of avoiding spectral overlaps blocks yet more. Further, complex layers of target priorities make it difficult to identify underlying bias, let alone to reconstruct unbiased samples, with a few exceptions (e.g. E. Curtis-Lake et al. 2025; A. Graaff et al. 2025). Conversely, slitless spectroscopy achieves higher multiplex and substantially better practical completeness – every source in the field can be observed simultaneously, at the expense of potential source confusion. However, with nothing blocking the background from the regions of sky without targets, the sensitivity is reduced significantly. Further, NIRCam and NIRISS grisms cover much narrower wavelength ranges per exposure. Hence, there has been a trade-off between spectral coverage, sensitivity, and multiplexing.

Attempting to increase the MSA allocation efficiency has led to experiments that combine NIRSpec prism spectroscopy with overlapping grating spectroscopy (A. J. Bunker et al. 2024; M. V. Maseda et al. 2024; A. Graaff et al. 2025; D. J. Eisenstein et al. 2026). Because the prism spectral traces are shorter than those for the gratings, these works have relied on the prism to disentangle overlapping sources. Here we present a hybrid approach that we believe offers improved efficiency for programmes focused on emission lines from large samples of faint galaxies. Simply put, we drop the prism requirement, and focusing on the NIRSpec gratings we open slits on every target object that has usable centration in its slit. Typically, this results in the overlap of 5–10 spectra, but this is of little consequence, because the dispersed background, even in the $R = 1000$ gratings is still fainter than detector noise. Because emission lines occupy a tiny fraction of the spectral footprint compared to continuum light, overlap of the lines is rare. We avoid targets bright enough that their dispersed continua would exceed the detector noise and thereby degrade statistical precision on other lines. This approach increases targeting density by factors of 4–5 compared to standard approaches while preserving the sensitivity advantages of slit spectroscopy.

Given the overlap of spectra, one must successfully associate the detected lines with the correct target. This is the same problem as with slitless spectroscopy, but now with even fewer candidates (since non-targets are masked). There are many paths to success. First, the detection of multiple well-separated lines immediately indicates the location of the source. Secondly, the astrometric location of sources along the slit is quite diagnostic: a 3-shutter slit is 15 pixels high, so requiring an astrometric match to even a few pixels is an 80 per cent rejection of false positives. Finally, one typically has photometric redshifts that inform the plausibility of line associations.

Clearly, a requirement for this mode is to have adequate preimaging for target selection and astrometric alignment. This is now available in many well-studied deep fields (e.g. S. L. Finkelstein et al. 2023; R. Bezanson et al. 2024; D. J. Eisenstein et al. 2025, 2026). One of the commonly expressed advantages of slitless spectroscopy is the serendipitous discovery of emission lines. However, we note that if a line can be detected in a slitless grism exposure, with the full background noise plus the signal losses from the disperser, then it will be detectable in a direct image in the same filter and exposure time, even without any boost from the continuum. Indeed, emission lines are routinely detected in deep multiband NIRCam imaging, and such sources could be included in the target lists.

In this paper, we present the results of an on-orbit pilot observation in which we use a single MSA configuration to target all faint galaxies with photometric redshift above 3, reaching 30th magnitude in *F444W*. Of the ∼2500 targets in the MSA footprint, ∼850 were observed on a single configuration, and we obtained secure redshifts for 539 of these. Unlike single-filter grism spectra, these spectra cover a wide wavelength range (1.6–5.3 μm with two gratings), and hence are useful for analyses that require multiple emission lines. Because the background is dispersed, the line detection limits are much fainter than with a wide-band grism, about a 5-fold decrease in error or 25-fold decrease in exposure time.

Our scientific purpose in these observations was to augment the spectroscopic coverage of the JADES Origins Field (JOF; D. J. Eisenstein et al. 2025), a deep field embedded in the broader JADES survey of the GOODS-S Field (M. J. Rieke et al. 2023; A. J. Bunker et al. 2024; D. J. Eisenstein et al. 2026). The JOF has exceptional NIRCam coverage, with 15 filters totalling about 350 h of exposure time. A partially overlapping NIRCam pointing from the OASIS programme (Observing All phases of StochastIc Star formation; PIs: Looser & D'Eugenio, program ID 5997) extends the region of medium-band coverage. Given this imaging resource, we particularly sought to focus on galaxies above redshift 3, where the high equivalent width H α and [O III]λ5007 lines can yield spectroscopic redshifts even for very faint galaxies. The spectroscopic measurements of redshift, line fluxes, metallicities, dynamics, AGN markers, and environment greatly complement the spectral energy distribution (SED) and morphological measurements coming from this deep field.

This paper is organized as follows: We start by presenting the survey design, target selection (Section 2), and the data reduction (Section 3). We then move to the redshift and flux measurements (Sections 4 and 5), before showcasing the potential of our novel approach through a series of science highlights (Section 6). We discuss the current performance and future outlooks of this 'Dark Horse' survey (Section 7), and we conclude with a summary of our findings (Section 8).

Throughout this work, we assume the flat λ Cold Dark Matter cosmology from Planck Collaboration VI (2020). All stellar masses assume a G. Chabrier (2003) initial mass function. We adopt the solar metallicity $12 + \log(\mathrm{O/H}) = 8.69$ (M. Asplund et al. 2009). All magnitudes are in the AB system (J. B. Oke & J. E. Gunn 1983). All wavelengths are vacuum wavelengths (but we use air wavelengths when reporting the name of optical emission lines).

2 SURVEY DESIGN AND TARGET SELECTION

2.1 Observations

The Pilot Survey to showcase dense-shutter spectroscopy is Dark Horse, which is based on observations from *JWST* PID 3215 (PIs: D. J. Eisenstein and R. Maiolino). A fraction of PID-3215 Cycle-2 observations failed due to MSA shorts and were re-allocated as compensation in Cycle 3. However, when these

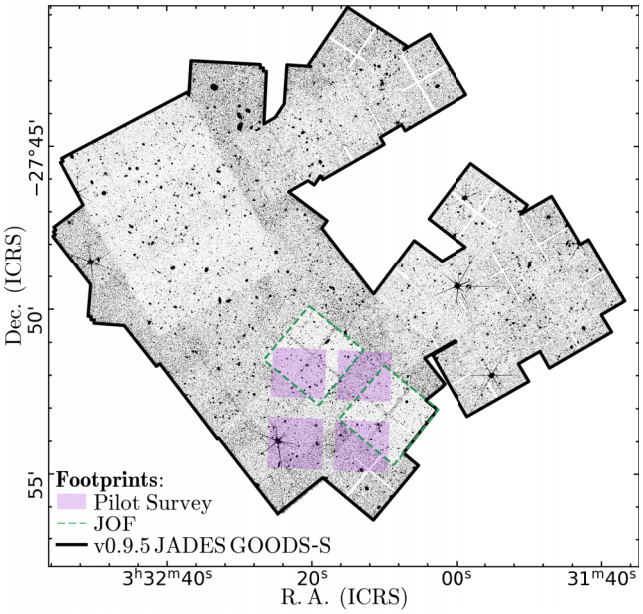

Figure 1. Position of the Dark Horse pilot survey pointing (shown in pink) in relation to existing multiband NIRCam coverage from JADES (solid black) and to the deep JOF field (dashed green). The NIRCam mosaics are from B. E. Robertson et al. (2026).

replanned observations were lost to a telescope safing, implying a further year of delay, we redesigned the observations to target the JOF and provide dense spectroscopy of the emission-line targets there. The position of the final pointing is illustrated in Fig. 1.

To focus on rest-optical lines at $z > 3$, we use the G235M and G395M gratings. These $R \sim 1000$ medium resolution gratings sufficiently disperse the background and target continua so that one can overlap many spectra, but they only marginally resolve the emission lines of normal galaxies, with a limited drop in emission-line signal-to-noise ratio (SNR) in comparison to the detector noise level. They also provide the nominal wavelength coverage, save the gap between the two NIRSpec detectors, for any location in the MSA, and they are able to split several useful emission-line groups. These include He Iλ1640 and O III]$\lambda\lambda$1661,1666, H γ and [O III]λ4363, H α and [N II]$\lambda\lambda$6548,6583, and [S II]λ6716 and [S II]λ6731.

The spectroscopic observations were obtained as Observation 901 on 2024 Dec. 17–18. They consist of a single MSA configuration with a 3-nod pattern, repeated several times with both gratings. Nodding further reduces the Dark Horse multiplexing, by requiring one functional shutter above and one below the allocated source; however, for Dark Horse, we adopted this approach to help design and evaluate a master background subtraction in the future. The two dispersers received 9.3 and 10.0 h on source, respectively. These were distributed in four identical sets of three nodded exposures each, with 19 groups per integration and 2 integrations per exposure, using the `IRS²` readout (B. J. Rauscher et al. 2012) and totalling 8403 s for each of the four sets. We note that long integrations, here 1400 s, are preferred to suppress detector noise (S. M. Birkmann et al. 2022). The G395M also had a single set of three nodded exposures, with 10 groups and one integration, totalling 2232 s, to finish using the available time allocation.

The resulting data set is very deep, with 33.6 and 35.8 ks of exposure in G235M and G395M, respectively. We chose to concentrate our observing time on a single deep MSA configuration rather than splitting across multiple shallower pointings to maximize sample size. This strategy leveraged the exceptional depth of the JOF imaging to probe faint galaxy populations while allowing us to test the method's limits for data reduction and deblending of faint lines. This depth also distinguishes the new data set from the 4 JADES Medium/*JWST* pointings in the same area (E. Curtis-Lake et al. 2025; J. Scholtz et al. 2025), each with 9.3 ks of exposure in these dispersers. Within JADES, only the two deep pointings, each of 25 ks per disperser, and the 3215 ultra-deep pointing with 160 ks in G395M are of comparable or deeper depth. The Deep/*JWST* pointing (programme 1287) is located on the JOF; the other two are elsewhere, on the Hubble Ultra Deep Field.

2.2 Target selection

The target selection in the Pilot Survey is chosen to maximize coverage at $z > 3$ while being unhesitant about using the high multiplex to push to the faint galaxies available in the JOF. From the JADES catalogue version v0.9.5 (F. D'Eugenio et al. 2025b), we require a 7-σ detection in any of *F277W*, *F335M*, *F356W*, *F410M* or *F444W* inside a circular aperture of radius 0.15 arcsec. To minimize detector artefacts, we also require a 7-σ detection in the short-wavelengths stack, constructed by adding *F090W*, *F115W*, *F150W*, and *F200W*. This enables selection to very faint levels, as faint as 3 nJy in the JOF and 8 nJy in the flanking JADES Medium imaging (16th percentile; the sample medians are 13 and 27 nJy, respectively). Although this is very faint, the anticipated line-flux limit around 2×10^{-19} erg s^{-1} cm^{-2} would itself be only a 1 nJy contribution to a NIRCam wide-band. Such a line at 3 microns in a source with a flux of 3 nJy would have an observed equivalent width of 2000 Å corresponding to a rest-frame equivalent width of 440 Å in H α or 330 Å in [O III]λ5007; these are routine values at high redshift (R. Endsley et al. 2023; K. Boyett et al. 2024). This calculation reinforces the point that the strong lines at high redshifts allow *JWST* slit spectroscopy to keep pace with the deep imaging.

For the redshift cut, we use EAZY photometric redshifts (G. B. Brammer, P. G. van Dokkum & P. Coppi 2008) obtained as described in K. N. Hainline et al. (2024). We impose $z_{\rm phot} > 3$ and redshift uncertainty $\sigma_z/(1+z) < 0.1$, where $z_{\rm phot}$ is `z_a` and σ_z is `u68−l68` from the updated catalogue of K. N. Hainline et al. (2024). We stress that the medium-band imaging available in this field combined with the strong lines of high-redshift galaxies tends to yield unusually accurate photometric redshifts; of course, we can test this after the fact, as presented in Section 4.2.

In dense-shutter mode, avoiding bright sources is essential, because the wide spectral coverage of the long-pass filters means that spectral overlaps have a long footprint in the dispersion direction of the detector. To reject bright continuum sources, we require that the minimum flux between *F277W*, *F356W*, and *F444W* is $F_\nu < 300$ nJy (AB mag 25.2). This use of minimum seeks to avoid the rejection of galaxies with strong emission lines that might boost 1 or 2 filters. This removes 2.5 per cent of the targets from the parent sample. Unfortunately, two stars were also included by this selection, because they mimic F090W dropouts (providing high-precision, inaccurate redshifts) and their red flux is already in the Rayleigh-Jeans tail, eluding our continuum flux cut.

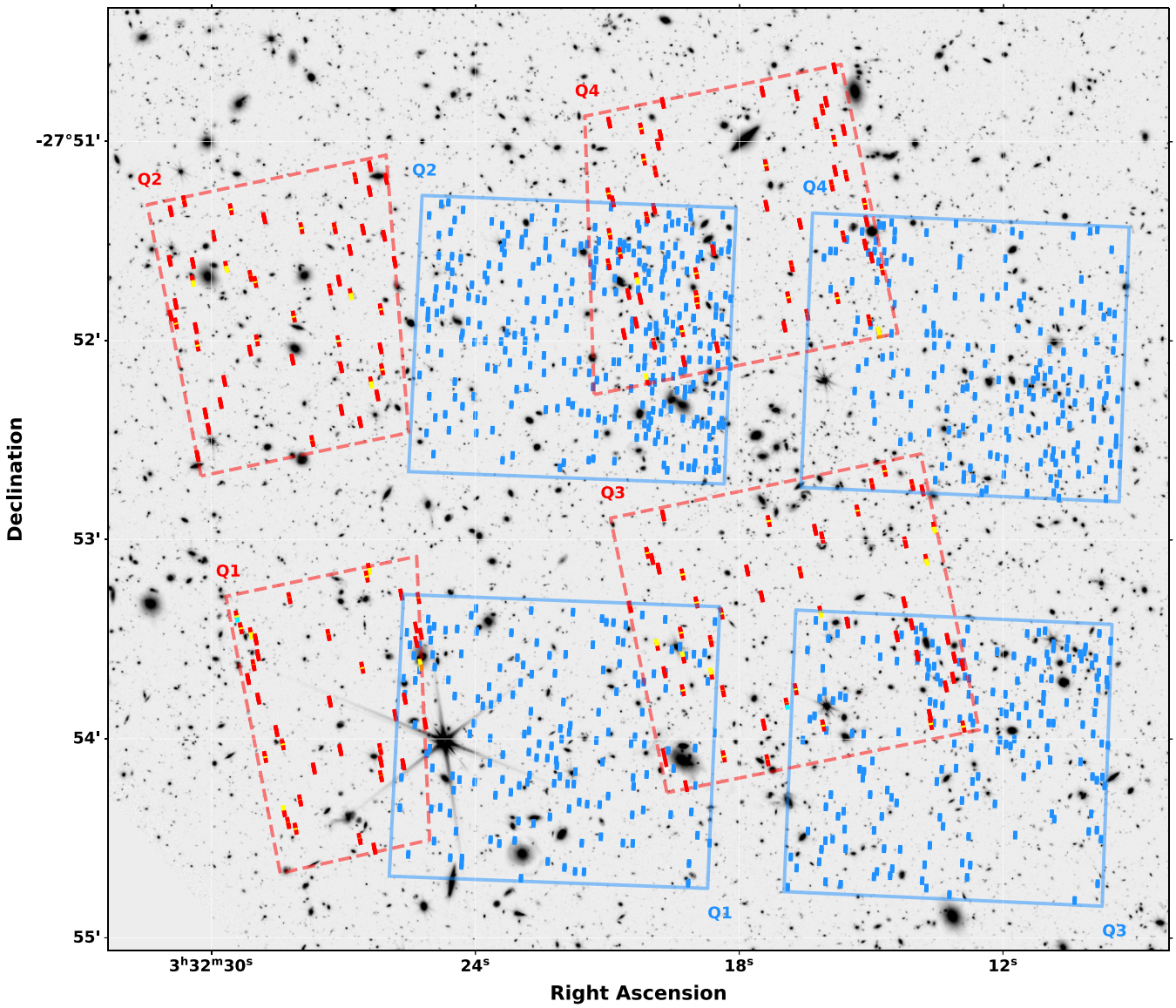

Figure 2. Comparison of a standard MSA target allocation allowing only moderate spectral overlaps (red slitlets; from PID 1287, E. Curtis-Lake et al. 2025), and the dense-shutter method presented in this paper (blue). Both configurations use 3-shutter slitlets. The outlines of the individual MSA quadrants are shown as solid lines for Dark Horse and dashed lines for the standard MSA setup used in PID 1287. The shape of the latter reflects the mask design used by JADES to avoid truncated PRISM spectra, while Dark Horse uses the standard `NRS_VIGNETTED_MSA` aperture. The background image shows a stacked F356W mosaic (B. E. Robertson et al. 2026).

Most selected sources have weight 1 for MSA design. However, to ensure a guaranteed science return in this experimental observation, we upweight a number of promising sources, giving them weight 10. These consist of 'Little Red Dot' AGN candidates (LRDs; J. Matthee et al. 2024) and $z > 7$ galaxies from K. N. Hainline et al. (2024). A single notable source, JADES-GS-z13-1-LA (J. Witstok et al. 2025, NIRSpec ID 13731) was allocated manually, with weight 100. This galaxy is a remarkable Lyα emitter spectroscopically confirmed at $z = 13.1$ with the *JWST*/NIRSpec prism, so our observations provide increased depth to attempt a detection of Lyα and rest-frame UV lines in the gratings (J. Witstok et al. 2026). After the allocation procedure, we assigned 854 targets for observation, of which 28 targets are located in already occupied slitlets. The location of allocated slitlets is shown in Fig. 2. For targets with weight 10, the allocated fraction was 26/42, 1.8 times higher than unweighted targets.

In Fig. 3, we show the allocated sample as well as the objects for which we were able to obtain spectroscopic redshifts, reaching levels of 2–3 nJy.

In Section 2.4, where we evaluate the effect of spectral overlaps, we also consider the photon noise added by overlapping source spectra. For this, we use the typical brightness of the allocated targets, measured inside circular apertures of 0.15-arcsec radius. The aperture area is 20 per cent smaller than the open area of a shutter, but this is compensated by the fact that shutters (0.2-arcsec width) enclose only 80 per cent of the circle's area. To estimate the continuum, we use the minimum (considering both detected fluxes and 3-σ upper limits) among *F150W*, *F200W*,

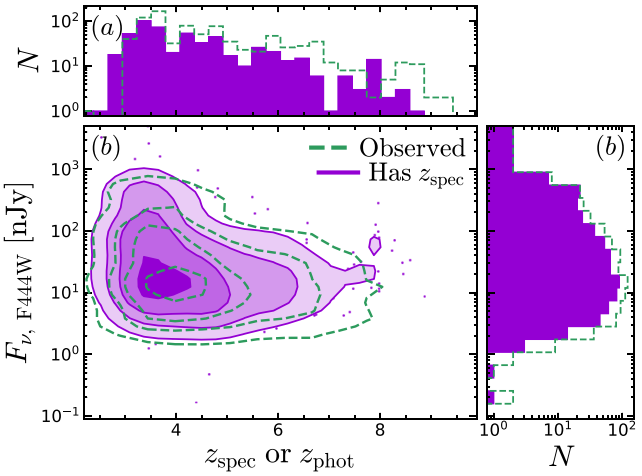

Figure 3. Distribution of the Pilot Survey galaxies in the redshift–magnitude plane (dashed green), compared to the subset that had successful spectroscopic redshifts (purple). Dots are individual sources outside the outermost contour. We stress the high-success rate to even 3 nJy continuum sources.

F277W, *F335M*, *F356W*, *F410M*, and *F444W*. This yields flux densities of 14 nJy (mean) and 5 nJy (median). Using the mean flux density in each filter, we would get higher values ranging between 25–40 nJy in the filters above. This estimate is 2–3 times higher than the previous; the difference is a combination of spectral slopes and emission-line contribution.

2.3 Allocation efficiency and completeness

The completeness of the single Dark Horse configuration is $f_{\rm C} = 0.34$: we allocate 854 sources out of 2516 targets within the four-quadrant footprint of the MSA (i.e. ignoring the 23-arcsec Q1–Q3 gap and the 37-arcsec Q3–Q4 gap). Such completeness is remarkable, given that the maximum completeness reached in the JADES Medium/*JWST* survey – for much brighter targets with lower number density – is $f_{\rm C} \sim 0.45$, which required multiple overlapping pointings (E. Curtis-Lake et al. 2025). Three effects set $f_{\rm C}$: vignetting by the MSA bars ($f_{\rm V} = 0.64$), inoperable-shutters fraction coupled with the three-shutter slitlet requirement ($f_{\rm F} = 0.60$), plus a user-defined exclusion zone around allocated targets (4 shutters in the dispersion direction; $f_{\rm X} \approx$ 0.80-0.90). So $f_{\rm C} \simeq f_{\rm V} \times f_{\rm F} \times f_{\rm X}$. We now proceed to estimate each term.

We evaluate these three terms at the actual pointing, because the JOF is very deep, with over twice the target density of the surrounding JADES field (after selection, $\rho_{\rm JOF} \approx$ 350 arcmin^{-2} versus 150 arcmin^{-2}). At the assigned position angle 177.57° and at the final NIRSpec pointing (R.A., Dec.) = ($3^{\rm h}32^{\rm m}7.50^{\rm s}$, $-27°53^{\rm m}2.71^{\rm s}$), we select 2516 targets across the four MSA quadrants, of which 1516 are in the JOF (4.3 arcmin^2; 38 per cent of Dark Horse) and 1000 in the shallower flanking field.

To limit aperture losses, we accept sources whose centre falls within the open-shutter area, i.e. the inner 64 per cent of the 0.27 × 0.53 arcsec^2 microshutter area (`entire_open` setting in MPT; MSA Planning Tool, D. Karakla et al. 2014). This downscales the allocatable counts to 975 (JOF) and 643 (non-JOF).

Not all shutters are operable, and forming three-shutter slitlets further reduces availability. We calculate the average usable-shutter fraction to be $f_{\rm F} = 0.60$, which yields 589 and 388 expected allocations in the JOF and flanking field, respectively, for a total allocatable source count of 977.

While we allow spectral overlaps, MPT still requires a minimum intersource spacing of four shutters along the dispersion direction. This sets an effective 3 × 9-shutter exclusion box, inside which only one slitlet can be opened. To estimate the impact of this exclusion box, we use two approaches. First, we estimate $f_{\rm X}$ by using the exclusion-box area of 3.86 arcsec^2 (equivalent radius 1.1 arcsec) to identify targeting conflicts. Of the 1516 candidates in the JOF, 849 have no neighbour within 1.1 arcsec; the remaining 667 have, on average, 1.6 neighbours. For simplicity, we assume that we can assign only half of these sources, 667/2. We thus estimate 849 + (667/2) = 1183 allocatable targets. Outside the JOF, 684 candidates are isolated; the remainder average 1.4 neighbours, for 842 effective targets. We thus estimate the allocation completeness due to the exclusion box to be $f_{\rm X} = (1,183 + 842)/2,516 = 0.80$. As a sanity check, we can compare the number of sources inside the acceptance region of operable shutters (977, estimated earlier) to the actual allocated number of 854; this gives $f_{\rm X} = 0.9$. The fact that this number is actually higher than the first estimate suggests that there are no other significant contributions to the efficiency of the target allocation. The discrepancy between the two estimates can be due to the simplification of assuming we observe only half of the sources with neighbours.

These factors vary with assumptions. $f_{\rm X}$ depends on the exclusion-zone size and survey depth; we measure $f_{\rm X} \approx 0.85$ in the JOF and $f_{\rm X} \approx 0.91$ outside. The 2× higher target density in JOF more than compensates for the drop in $f_{\rm X}$, yielding more allocations per unit area. $f_{\rm V}$ reflects the accepted in-shutter area and can approach 1.0 if positional constraints are relaxed. Finally, $f_{\rm F}$ depends on operable-shutter statistics and slitlet length. With the current operability mask, one- and five-shutter slitlets result in $f_{\rm F} = 0.74$ and $f_{\rm F} = 0.5$, respectively. In addition, the slitlet size also affects the MPT exclusion box. For reference, single-shutter observations (dropping nodding) would shrink the exclusion box (from 3 × 9 to 1×9 shutters). For our parent sample, this raises the calculated $f_{\rm X}$ from 0.8 to 0.88-0.92. Together with the increased $f_{\rm F} = 0.74$, this would yield $f_{\rm C} \approx 0.40$, roughly 30 per cent more targets per MSA configuration than this pilot survey.

2.4 Spectral overlaps

To calculate the penalty due to spectral overlaps, we compare the standard noise terms in standard MSA spectroscopy, background and detector noise, to the additional noise due to spectral overlaps.

Each 1400-s integration with `IRS`^{2} readout incurs detector noise $\sigma_{\rm IRS^2} \approx$ 6.3-7.4 e$^-$ (S. M. Birkmann et al. 2022, interpolated from their table 3). This term also includes noise due to dark current. This is generally the dominant noise term for faint-object grating spectroscopy with NIRSpec/MSA.

The second important noise source is photon noise from the sky background. In December, JOF incurs $\mu_{\rm B} \approx$ 66-130 nJy per NIRSpec detector pixel at $\lambda =$ 2-4.5 μm, appropriate for 0.1-arcsec pixels and 0.2-arcsec wide shutters (J. Rigby et al. 2023). The additional photon noise per pixel corresponds to $\sigma_{\rm F} =$ 2-3.7 e$^-$, where we have used

$$\sigma_{\rm B}^2 \equiv \mu_{\rm B}\ \frac{\rm c}{\lambda^2}\ \Delta\lambda\ \left(\frac{\rm c\,h}{\lambda}\right)^{-1}\ A\ {\rm PCE}(\lambda)\ \Delta t, \qquad (1)$$

where $\Delta\lambda \approx$ 6-17.6 Å is the size of a NIRSpec detector pixel, A is the telescope area, and $\Delta t = 1,400$ s is the integration time. The photon-to-electron conversion efficiency PCE also includes optical telescope element (OTE) losses; we use the values based on in-flight measurements (G. Giardino et al. 2022).

Finally, we estimate the photon noise from the continuum, which given our mean flux density of 14 nJy (Section 2), amounts to $\sigma_S = 1.5$-2.0 e^- (equation 1). We assume this extra noise is spread in the spatial direction in the same manner as the main source, and we do not account for second- and higher-order spectra, whose contribution to the noise is lower (though in this pilot survey some rows are affected by bright targets).

Our reference noise is thus $\sigma^2_{\rm MSA} = \sigma^2_{\rm IRS^2} + \sigma^2_B + \sigma^2_S$ (see also equation 2 below).

In Dark Horse, 854 targets opening 2562 shutters in the 342 rows of the MSA, corresponds to an average of $N_{OB} = 7.5$ overlapping background spectra per pixel on the detector. So overlaps cause an effective background μ_{OB} which is 7.5 times higher than the standard background μ_B. This is a conservative estimate: for G235M, the reddest end of the wavelength range after 3.2 μm is significantly fainter, due to the grating efficiency decreasing away from blaze wavelengths. For G395M, the detector efficiency drops to zero at $\lambda \gtrsim 5.5$ μm, hence the spectral traces are noticeably shorter than a detector, and the effective overlap should be 2× lower than for G235M. In practice, since the outer 1/3 of both NRS1 and NRS2 is unused, the G395M traces are distributed effectively over 2/3 of the total detector area, hence the effective overlap in G395M is $7.5/(2 \times 2/3) = 5.6$, where the factor 2 represents the spread over two detectors. For the rest of the article, we ignore this difference in the interest of simplicity.

Overlapping spectra also incur additional photon noise from overlapping sources. With 854 targets over 342 rows and two detectors, the number of source overlaps per shutter is $N_{OS} = 2.5 = N_{OB}/3$, so $\mu_{OS} = 2.5\,\mu_S$, where we divide by three since each 3-shutter slitlet contains typically only one source.

Overall, the noise ratio between dense-shutter and standard MSA can be estimated from

$$\frac{\sigma^2_{\rm DH}}{\sigma^2_{\rm MSA}} = \frac{\sigma^2_{\rm IRS^2} + N_{OB}\,\sigma^2_B + N_{OS}\,\sigma^2_S}{\sigma^2_{\rm IRS^2} + \sigma^2_B + \sigma^2_S} = 1 + \frac{(N_{OB}-1)\,\sigma^2_B + (N_{OS}-1)\,\sigma^2_S}{\sigma^2_{\rm MSA}}. \quad (2)$$

By comparing $\sigma_{\rm IRS^2}$, σ_B, and σ_S, we conclude that in dense-shutter spectroscopy the dominant noise source is still detector noise, just like in non-overlapping NIRSpec spectroscopy. This outcome depends on our configuration, sample properties, and background. With our mean target brightness, it is not until an average overlap of 10 (30 per cent larger than our allocation) that the overlap noise reaches a level comparable to the detector noise. Conversely, holding constant the degree of overlaps, one needs a mean sample brightness of 120–280 nJy in *F277W–F444W* before the overlap noise due to the sources reaches the detector noise. Finally, while background noise is generally subdominant in NIRSpec grating spectroscopy, this can change when combining many spectral overlaps with higher background, e.g. in fields close to the Ecliptic.

With our same-pixel background subtraction strategy, based on three nods, one must further add the photon and detector noise due to the subtracted background, which are only $\sqrt{2}$ lower than for the pixel under consideration. This further reduces the gap between dense-shutter spectroscopy and non-overlapping allocations.

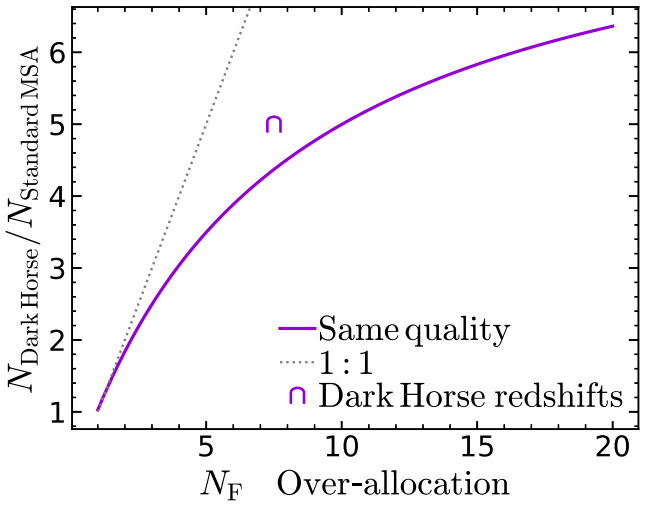

Figure 4. Number of sources in dense-shutter mode relative to standard MSA allocation, requiring the same sensitivity, and correcting dense-shutter for the exposure time penalty due to spectral overlaps. Since overlaps incur higher photon noise (in our case, primarily from the background), achieving the same data quality requires longer integration, increasing with the square-root of the number of allocated sources. In practice, confusion will eventually cause a maximum in the curve. The single data point is the empirical estimate from Dark Horse, based solely on the number of successful redshifts (Section 4).

With our mask design – and ignoring subdominant noise terms – the increased noise in dense-shutter spectroscopy corresponds to a single-source time penalty factor of $(\sigma_{\rm DH}/\sigma_{\rm MSA})^2 \approx 1.7$ relative to non-overlapping MSA spectroscopy. This estimate is validated empirically in the next section. At the blue and red ends of the wavelength range, the time penalty increases: 2.5 at $\lambda =$ 1.5 μm and 2.8 at $\lambda = 5.3$ μm; this is due to the increasing sky background, which means these wavelengths approach the background-dominated regime with fewer spectral overlaps than 2–4 μm. In any case, accepting this penalty is extremely advantageous, due to the large increase in sample size, resulting in remarkably faster survey speed (Fig. 4 and Section 4). Fig. 4 shows the factor increase in sample size as a function of how many overlaps one allows. This calculation takes account of the increase in noise as a result of overallocation, thus giving an indication of the gain in efficiency allowed by dense-shutter.

3 DATA REDUCTION

The data reduction procedure followed the standard methods developed by the JADES collaboration, based on work by the ESA NIRSpec Science Operations Team. The original algorithms have been extensively updated, as described in the JADES spectroscopic data-release articles (A. J. Bunker et al. 2024; J. Scholtz et al. 2025; F. D'Eugenio et al. 2025b). The static calibrations used are based on the context file version 1413. The current pipeline does not automatically reduce objects falling in background shutters (28/854 sources). We perform nod background subtraction and point-source path-loss corrections. We refer the reader to the JADES Data Release 4 article for more information (J. Scholtz et al. 2025). Separately, we also perform a reduction with no background subtraction, to assess the feasibility of such a

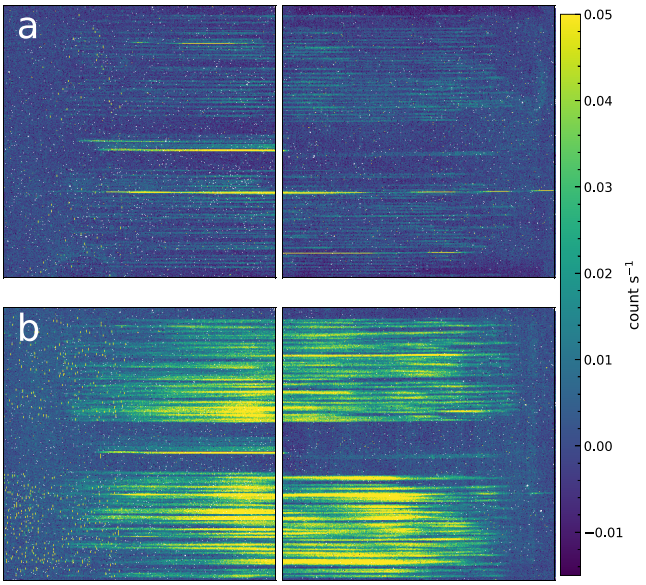

Figure 5. Count-rate maps from PID 3215 Obs 1 (a) and Dark Horse (PID 3215, Obs 901; b). The two observations use the same integration per exposure (Section 2), but each mask in Obs 1 allocates ∼150 targets, while Dark Horse allocates 854. The significantly higher target density of the dense-shutter comes at the cost of a somewhat brighter background. The bright spots on the left half of the NRS1 detector are zero-order slit images.

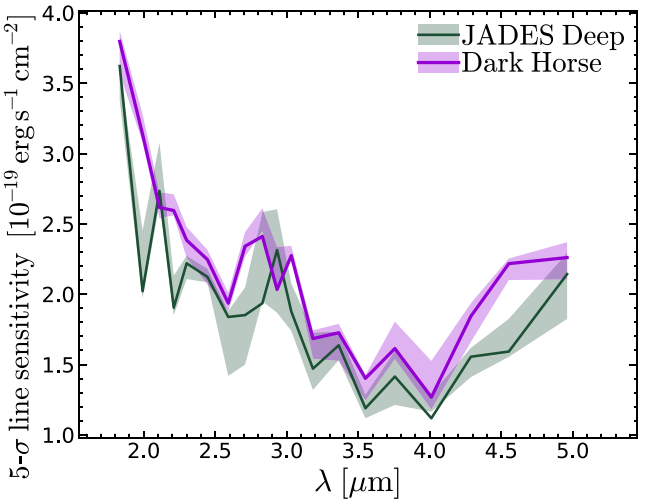

Figure 6. The emission-line sensitivity of dense-shutter spectroscopy (purple) is comparable to that of traditional NIRSpec/MSA observations of similar exposure time from JADES Deep (green). The curves show the 5-σ sensitivity in a 3-pixel boxcar extraction, estimated as the median of the noise, while the shaded regions spans the 16th–84th interpercentile range. JADES Deep used slightly shorter integration times; for an equal-time comparison see Section 7.1.1.

strategy for emission-line science surveys (Section 5). To illustrate the target density, we show a reduced detector image in Fig. 5, where we compare a G235M observation from a standard MSA configuration (Fig. 5a) to the Dark Horse observation (Fig. 5b).

The resulting 5-σ emission-line sensitivity is shown in Fig. 6 (purple curve). This value is measured from the emission-line flux and flux error of all detected emission lines (SNR $>$ 3), measured inside a 3-pixel boxcar extraction. We consider only lines from galaxies with redshifts. The sensitivity is obtained by grouping the emission lines in twenty wavelength bins with equal numbers of lines, then for each wavelength bin i we fit the flux error with the formula $\sigma_{\mathrm{F},i} = \sqrt{s_j + a_j \cdot F_i}$, where F_i and $\sigma_{\mathrm{F},i}$ are the flux and flux error of the ith emission line in the jth wavelength bin, while a_j and s_j free parameters. We then define the sensitivity as $5 \times s_j$, under the reasonable assumption that the photon-noise term $a_j \cdot F$ is subdominant near the sensitivity limit of our deep observations. The uncertainties are calculated for each bin by bootstrapping the emission lines in that bin. We validate this method against sampling the background noise in random, line-free apertures (e.g. D. J. Eisenstein et al. 2026), and find good agreement. For reference, we use the same method to calculate the sensitivity from traditional MSA observations with fewer overlaps (green; PIDs 1210, A. J. Bunker et al. 2024 and 1287, J. Scholtz et al. 2025); these deep observations from JADES have comparable exposure time to Dark Horse, enabling a direct performance evaluation. The empirical noise penalty is 13 per cent, calculated as the median ratio between Dark Horse and JADES deep. This value is comparable to the estimated exposure-time penalty from Section 2.4. There, we estimated dense-shutter to require 1.7 longer exposures to achieve the same sensitivity as standard MSA. After accounting for the longer actual integration of Dark Horse versus PIDs 1210 and 1287 (33 ks versus 25 ks), we obtain an estimated noise increase of 1.14 ($\sqrt{1.7 \times 25 \div 33}$), meaning that our knowledge of the instrument and sample enable accurate prediction of the dense-shutter performance.

4 REDSHIFT CATALOGUE

4.1 Redshift determination

The redshift measurements follow the procedures outlined in F. D'Eugenio et al. (2025b). These consist of an initial round of visual inspection, which uses a user-movable slider to refine or change the initial redshift guess, based on the photometric redshift from the input catalogue. This procedure is usually accurate to within a single spectral pixel.

Spectral overlaps are readily identified because they are not centred in the cross-dispersion direction, and/or the wavelengths of multiple emission lines are not consistent with any redshift solution (Fig. 7a), and/or if they are incompatible with the known SED from photometry (Fig. 7b). This outcome is fully consistent with the expectations based on the small detector footprint of emission lines. Examples of successful and unsuccessful measurements are shown in Fig. 8

Based on the visual-inspection redshift, we use the medium-resolution line-fitting pipeline (J. Scholtz et al. 2025) to fit a pre-defined set of emission lines, including hydrogen and helium recombination lines, nebular lines, and the auroral line [O III]λ4363. From these lines, we then define the spectroscopic redshift as follows. We establish a line priority, consisting of [O III]λ5007, Hα, Hβ, [S III]λ9532, He Iλ1.08μm, [Ne III]λ3869, Hγ, Paα, Paβ. For each target, we run through this list, and assign the redshift of the first line that has a SNR $>$ 5 detection. The resulting redshift table consists of 519 robust redshifts from multiline associations (and 105 tentative redshifts, identified in visual inspection from tentative emission lines, or from strongly detected single lines). This amounts to success rates of 63 (75) per cent.

After measuring the line fluxes, we identify 535 objects with emission-line detections above SNR $>$ 5, representing a success

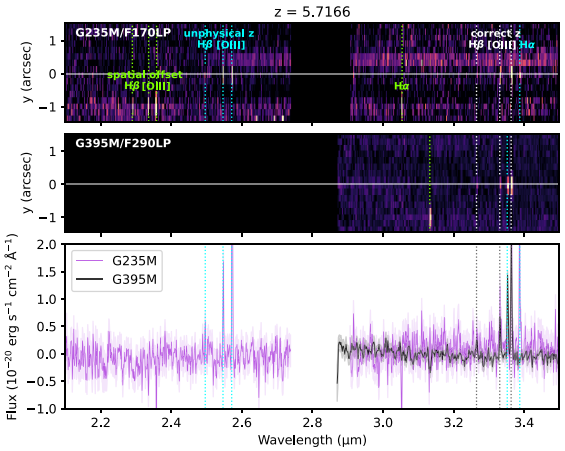

Figure 7. Example of spectral overlap identification. The 1D spectrum has two readily identified H β–[O III]$\lambda\lambda$4959, 5007 groups at 2.6 and 3.4 μm. In the 2D spectrum, $y = 0$ corresponds to the centre of the central shutter. The 2D spectrum shows additional H β–[O III]$\lambda\lambda$4959, 5007 emission near 2.3 μm. The latter is readily excluded due to its spatial offset from the middle of the central shutter. The group at 2.6 μm does not correspond to any redshift solution.

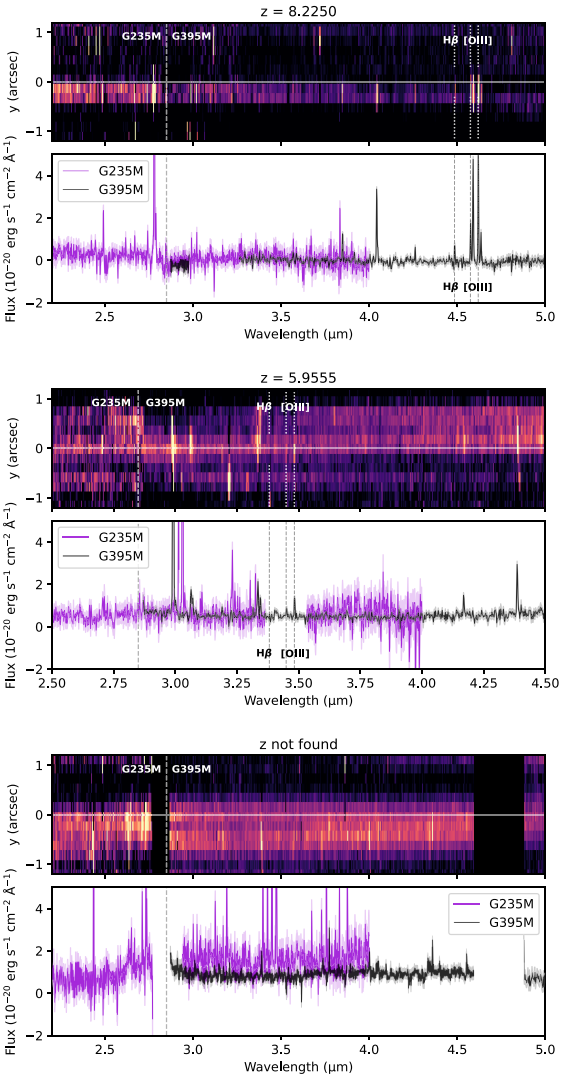

Figure 8. Three example overlaps showing a successful redshift (top), a rare example of emission-line overlap, i.e. a successful redshift with some corrupted line fluxes (H γ–[O III]λ4363; middle), and an example where no redshift could be measured (bottom).

rate of 65 per cent. As a benchmark, we can use the JADES deep pointing in the HUDF (PID 1210), which has similar gratings depth (A. J. Bunker et al. 2024), although their configuration also includes G140M and a three times longer exposure with the prism. For the comparison, we consider only galaxies with grating observations (198 of 253 targets), and take successful redshift measurements as those with redshift flag 'A', yielding a success rate of 103/198 or 52 per cent (A. J. Bunker et al. 2024). Of course, being constrained by avoiding prism spectral overlaps (and grating spectral overlaps for primary sources), the A. J. Bunker et al. (2024) result resorted to allocate a number of suboptimal 'filler' sources. Additional losses come from the fact that PID 1210 used three dithered pointings, resulting in a distribution of integration times between one third, two thirds, and the full exposure time. This complication underscores the difficulty of preserving high allocation efficiency in a single MSA configuration – another advantage of Dark Horse.

Overall – comparing just the grating observations – the dense-shutter approach delivers 25 per cent higher success rate, and – crucially – five times more redshifts. This is also true for the high-redshift sources: PID 1210 delivered 9, 4, and 1 grating redshifts in the intervals $6 \leq z < 7$, $7 \leq z < 8$, and $z \geq 8$, respectively; the Dark Horse survey yields 34, 24, and 6. The resulting distribution of spectroscopic redshifts is shown in Fig. 3(a), and spans $2.5 \lesssim z \leq 8.86$.

Among the 202 redshift failures, we identify three main reasons.

(i) Approximately one third (60/202) are invalid targets: objects with unreliable redshifts due to contaminated photometry (by neighbours or diffraction spikes), objects that are overshredded regions of bright foreground galaxies, and parts diffraction spikes themselves. Of course, removing these objects from the pool of valid galaxies would increase the success rate to 81 per cent.

(ii) The second category of failed redshifts (63/202) are objects that are faint (<5 nJy), show some line excess in the photometry, but no detected emission lines at the expected location in the spectrum. The sensitivity of these spectra may have been suppressed by the increased background or by overlapping continuum. A better target selection without bright AGN or stars would likely recover some of these sources.

(iii) The final category of redshift failures (58/202) are objects with intrinsically weak emission lines. These are identified by visual inspection of the EAZY SED fits, where we identified clear Balmer breaks in the photometry and little or no emission-line photometric excess. Interestingly, this group of sources still enables compelling science (Section 6.5).

Finally, two minor classes of failed redshifts are objects where the main emission lines are lost due to nod subtraction of bright overlapping spectra (regardless of whether one uses all three nods or just two nods; 4 objects) and objects where the main emission lines landed on the detector gap (17 objects).

4.2 Comparison to photometric redshifts

As this is a sample of faint galaxies, with rather simple flux and photometric redshift cuts, it presents a good opportunity to test the photometric redshifts. This is particularly important

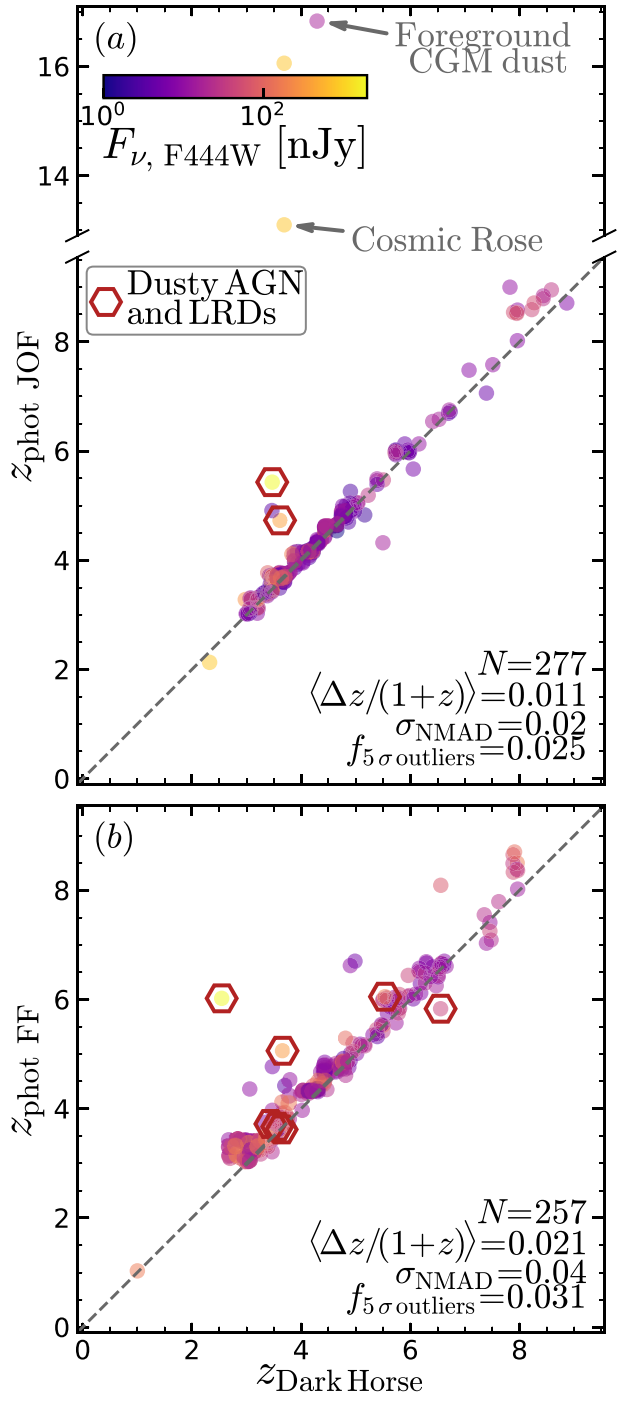

Figure 9. Comparison of the redshift accuracy in relation to photometry, splitting between the deeper JOF galaxies (a) and the shallower flanking field (b). Overall, the agreement is excellent, as quantified by the robust scatter measure σ_{NMAD} (see main text for the definition). Additionally, the few outliers are well understood, as explained in the text.

because the selection requires $z_{\mathrm{phot}} > 3$. Fig. 9 shows the comparison of our spectroscopic redshifts to the input photometric redshifts, split between the JOF (Fig. 9a), with deeper imaging and more complete filter set, and the flanking field (Fig. 9b). We find very good agreement, with modest bias (defined as the median of $\Delta z/(1+z)$), and 3 per cent 5-σ outliers – the latter driven by the extremely small dispersion σ_{NMAD}, calculated from the median absolute deviation and upscaled by the inverse of $\sqrt{2}\,\mathrm{erf}^{-1}(1/2) = 0.6745\ldots$, to match the relation between median absolute deviation and standard deviation in a Gaussian distribution (erf^{-1} is the inverse error function). The excellent agreement is a testament to the accuracy of the photometric input (K. N. Hainline et al. 2024). The JOF displays smaller bias and scatter by a factor of 2.

Catastrophic outliers are still present in both imaging subsets. These fall into three main categories: LRDs, dusty sources, and strong [O III]λ5007 emitters near $z_{\mathrm{spec}} = 8$. LRDs are generally difficult to obtain good photometric redshifts for; at $z_{\mathrm{spec}} \approx 3$, [O III]$\lambda\lambda$4959, 5007 and H$\alpha$ mimic a strong Balmer break with flat optical continuum. This difficulty is not limited to faint sources, as exemplified by GS-35453, a robust candidate quiescent galaxy at $z_{\mathrm{phot}} = 5.33$ (S. Alberts et al. 2024), which Dark Horse reveals to be an AGN at $z_{\mathrm{spec}} = 3.66$ (Section 6.6). Dusty galaxies generally lack both strong spectral breaks and high-EW lines capable of anchoring a redshift; they can appear as catastrophic outliers, but this difficulty is correctly reflected in their large confidence intervals. One of the notable outliers in the JOF is the 'Cosmic Rose' at $z = 3.69$ (S. Alberts et al. 2024; D. J. Eisenstein et al. 2026), the sub-mm galaxy ALESS009.1 (J. A. Hodge et al. 2013; J. E. Birkin et al. 2021). Even after 10 h on source, we still only detect the Hα–[N II]$\lambda\lambda$6548, 6583 complex, while Hβ and [O III]$\lambda\lambda$4959, 5007 remain undetected. Finally, there is a class of strong [O III]λ5007 emitters that suffer from a systematic bias of $\Delta z \sim 0.5$; these objects are characterized by strong *F410M*–*F444W* excess, and weak detection in *F090W*; the latter may be driving the redshift solution to $z \gtrsim 8$, and is perhaps connected to damped Lyα absorption (e.g. S. Fujimoto et al. 2023; Y. Asada et al. 2025).

Another notable outlier in Fig. 9(a) is GS-634005, a compact, red galaxy with a clear spectral break and a red SED. The nominal solution at $z_{\mathrm{phot}} = 16.8$ would imply high-dust attenuation and large stellar mass. Instead, a clear detection of Hα in NIRSpec places this galaxy at $z_{\mathrm{spec}} = 4.2918 \pm 0.0001$. The strong dust attenuation implied by the red SED is anomalous for such a compact, low-mass system, but the proximity to the sub-mm galaxy ALESS010.1 at $z = 3.47$ (separation 3 arcsec; J. A. Hodge et al. 2013) suggests we are witnessing foreground dust extinction in the circumgalactic medium (CGM) of ALESS010.1 (Section 6.3; F. Sun et al. 2026).

It is particularly remarkable that only two galaxies have spectroscopic redshifts below 2.5, indicating a very small rate of true low-redshift galaxies in the $z > 3$ input sample. We note that we would have detected the strong Hα line down to $z = 1.6$, and there are plenty of rest-infrared lines (e.g. [S III]λ9532 or Paα) that would have been in-band at lower redshift.

As a spectroscopic validation of our z measurements, we consider the 43 galaxies in common between the Pilot Survey and JADES DR4 (Fig. 10). Of these, 40 have valid redshifts in Dark Horse, and 36 have valid redshifts in JADES DR4. The agreement is consistent within better than a single spectral pixel, underscoring that – as far as redshifts are concerned – the dense-shutter multiplexing has no cost compared to low- or no-overlap NIRSpec/MSA spectroscopy. We note a single outlier, where we measure Paα at $z_{\mathrm{spec}} = 1.0012$ while JADES DR4 reports $z_{\mathrm{spec}} = 5.077\,89$. Both redshifts are accurate: This system is an LRD AGN at $z = 5$ plus a $z = 1$ interloper (F. D'Eugenio et al. 2026); the position of the MSA shutter in Dark Horse misses most of the LRD flux (even though faint [O III]λ5007 and Hα are still seen in the spectrum).

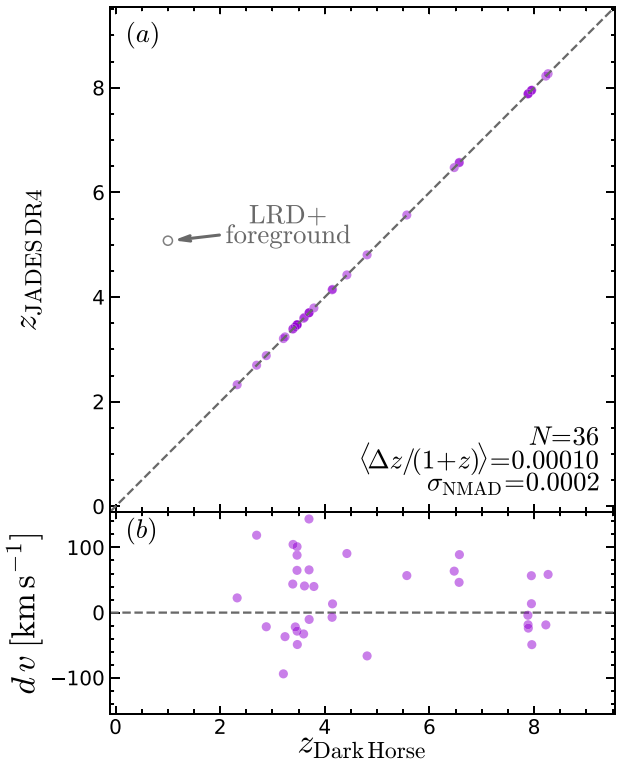

Figure 10. Comparison of the Dark Horse redshifts to known grating redshifts from JADES DR4. The agreement is within 10 per cent of a resolution element. The single outlier is due to foreground contamination inside the shutter.

5 FLUX MEASUREMENTS

The fluxes are measured using standard methods from the JADES Collaboration (J. Scholtz et al. 2025), consisting of a local Gaussian fit with a polynomial background. The list of lines considered is in Table 1. Groups of spectrally adjacent emission lines were fit simultaneously, using a common redshift and full width at half-maximum (FWHM) and the same continuum model; these line groups are also indicated in Table 1.

The depth of our observations is illustrated in Fig. 6, where we show the 5-σ emission-line sensitivity as a function of wavelength. The achieved depth is almost the same as what was obtained in the JADES deep pointings (green line). Overall, we demonstrate that the Dark Horse approach substantially increases the MSA multiplex with an acceptable penalty in sensitivity. We expect these conclusions to also apply to the higher-resolution gratings. In contrast, the prism may suffer from additional noise, due to its lower spectral resolution and higher continuum sensitivity; the exact performance of the prism in Dark Horse mode will be the subject of a dedicated article.

In Fig. 11 we gauge the accuracy of Dark Horse spectroscopy, using fluxes from JADES DR4 as a benchmark. We identify 43 galaxies in common between JADES DR4 and the Dark Horse pilot survey, which include 129 emission lines above a robust detection threshold of SNR > 5. The adopted SNR cut is applied to Dark Horse only, because the JADES DR4 sample includes targets from the medium-depth tiers, which received 1–2 h integration per grating, i.e. 5–10 times shallower than the Pilot Survey. This results in some line detections being only upper limits in JADES DR4. To identify systematic differences, we split the

Table 1. List of the emission lines. All wavelengths are in vacuum. Emission lines inside the same cell were fitted simultaneously using the same redshift, FWHM and continuum.

Line(s)	λ (Å)	Column name
C IVλλ1548, 1551	1549.48	C4_1549
He IIλ1640	1640.00	He2_1640
O III]λλ1661, 1666	1663.00	O3_1663
C III]λλ1907, 1909	1907.71	C3_1907
[O II]λλ3726, 3729	3728.49	O2_3727
[Ne III]λ3869	3869.86	Ne3_3869
H δ	4102.86	HD_4102
H γ	4341.65	HG_4341
[O III]λ4363	4363.44	O3_4363
H β	4862.64	HB_4861
[O III]λλ4959,5007	4960.30, 5008.24	O3_5007
He Iλ5875	5877.25	He1_5875
[O I]λλ6300,6364	6302.05	O1_6300
H α	6564.52	HA_6563
[N II]λλ6548,6583	6549.86, 6585.27	N2_6584
[S II]λλ6716,6731	6718.29, 6732.67	S2_6718, S2_6732
He Iλ7281	7283.36	He1_7281
[S III]λλ9069,9532	9071.10, 9533.20	S3_9069,S3_9532
Pa δ	10 052.12	PaD_10049
He Iλ10829	10 832.06	He1_10829
Pa γ	10 940.98	PaG_10938
Pa β	12 821.43	PaB_12818
Pa α	18 755.80	PaA_18751

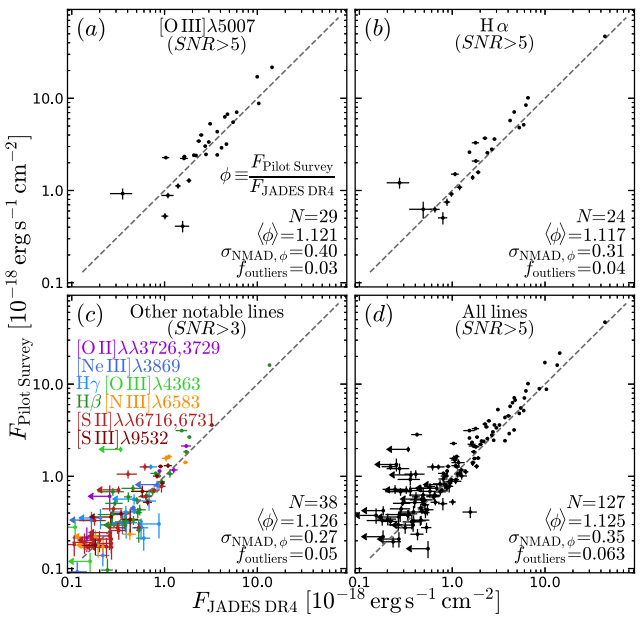

Figure 11. Comparison of the flux measurements from this work to those from JADES DR4, for 43 objects in common between the two surveys. The four panels show either individual lines ([O III]λ5007 and H α in panels (a) and (b), or a selected range of other notable emission lines (c), or all strongly detected lines together (d). In each panel, we report the number of emission lines above the specified detection threshold, the median flux ratio, the robust normalised median absolute deviation (NMAD) scatter about the median, and the fraction of 3-σ outliers. The results show excellent correlation; the 10 per cent flux discrepancy due to different path-loss corrections. We detect no bias between forbidden, permitted, or weak lines, which all agree with the trends observed in the full line data set. Dark Horse spectroscopy delivers high-fidelity line fluxes.

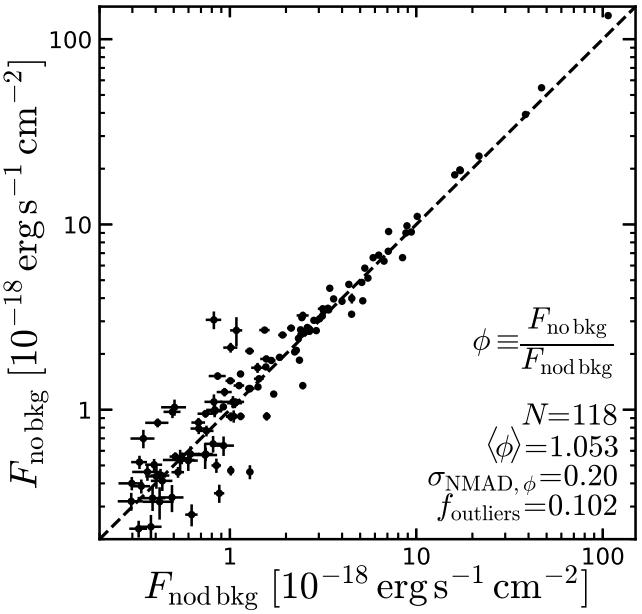

Figure 12. Comparison of the default flux measurements obtained using nod background subtraction to those obtained without removing the background, and using the emission-line fitting code to also model a local background. There is excellent agreement. At high fluxes, the alternative reduction without background subtraction yields higher fluxes, because it avoids self subtraction.

emission lines in four subsets: [O III]λ5007 is representative of strong forbidden lines (Fig. 11a); H α is representative of strong permitted lines, which can be broad in AGN (Fig. 11b). We then show a selected set of other emission lines; here we use a more generous threshold of SNR > 3, because these lines are generally weaker than [O III]λ5007 and H α in the mass and redshift range relevant here (Fig. 11c). Finally, we show all robust detections (Fig. 11d). Each panel reports the median of ϕ, the flux ratio between the Pilot Survey flux and the JADES DR4 flux, with the latter adopted as ground truth. We find 10 per cent higher flux in Dark Horse relative to JADES. This discrepancy correlates with both the intrashutter offset along the dispersion direction ($P = 0.01$) and anticorrelates with the observed line wavelength ($P = 0.03$). We attribute the discrepancy to the empirical path-loss corrections, which are reflection-symmetric along the cross-dispersion direction of the MSA, but not along the dispersion direction, thus explaining the correlation with the intrashutter offset in the dispersion direction only (see J. Scholtz et al. 2025, their Appendix B). The anticorrelation with wavelength is readily explained by the increasing size of the point spread function (PSF) with redder wavelengths. Over several pointings, this bias should be effectively random, but since we are dealing with single-pointing surveys and a small overlap of 43 galaxies, the fixed pitch of the MSA introduces this systematic trend.

As an alternative to the standard data reduction, we also analysed the emission-line fluxes without background subtraction, leaving it to the line-fitting algorithm to remove the background. The resulting line fluxes are shown in Fig. 12, where we find good agreement with the default data reduction. The systematic offset to higher flux is due to avoiding nod subtraction; this can happen in some faint sources, but is systematic for bright sources, due to self-subtraction of spatially extended sources. Overall, the agreement supports allocating even more microshutters, and using local methods or a model for background subtraction.

6 SCIENCE HIGHLIGHTS

Being a method to simply increase the emission-line yield of NIRSpec/MSA, Dark Horse naturally lends itself to most of the applications of standard NIRSpec/MSA spectroscopy. The only notable exception is continuum science, which includes stellar-population inference and equivalent-width measurements. Still, precise knowledge of the redshift and emission-line fluxes enables us to supplement and improve photometric constraints, which are available by design in Dark Horse. In the following we present a list of science highlights, using where relevant the JADES HUDF observations as a benchmark.

6.1 Star-forming main sequence

The pilot survey reports the 5-σ detection of 620 Balmer lines, between H α, H β, H γ, and H δ. These can be used to estimate accurate SFRs on short time-scales of 3–10 Myr (R. C. Kennicutt & N. J. Evans 2012), for instance using the scalings between H α luminosity and SFR from A. E. Shapley et al. (2023), which are appropriate for low-mass, metal-poor galaxies. Where multiple Balmer lines are detected, we estimate directly the dust attenuation, with the usual assumption of intrinsic Balmer ratios for case-B recombination (e.g. D. E. Osterbrock & G. J. Ferland 2006), electron temperature $T_{\rm e} = 10\,000$ K and electron density $n_{\rm e} = 500\,{\rm cm}^{-3}$ (Y. Isobe et al. 2023). Following M. Curti et al. (2023), we employ the extinction curve from K. D. Gordon et al. (2003, hereafter: G03) to infer the dust-attenuation $A_{\rm V}$. We measure 177 $A_{\rm V}$ values using the flux ratio H α/H β and 51 values using H γ/H β. This is comparable to or larger than other studies of the nebular attenuation at high redshift with *JWST* (A. E. Shapley et al. 2023; L. Sandles et al. 2024; C. Woodrum et al. 2025). For all other galaxies, we use the dust attenuation estimated from SED models obtained with the Bayesian tool PROSPECTOR (B. D. Johnson et al. 2021), using the public catalogue from C. Simmonds et al. (2025).

We illustrate the resulting star-forming main sequence (SFMS) in Fig. 13. Multiple Dark Horse pointings can deliver thousands of galaxies, which would enable dissecting the SFMS in redshift, $M_\star$ and environment – all while using a self-consistent selection function, high completeness, and slit-spectroscopy depth. Last but not least, the depth of the Pilot Survey enables studying galaxies below the SFMS, which we discuss in Section 6.5.

6.2 Gas-phase metallicity

JWST has revolutionized our knowledge of emission-line galaxies at epochs earlier than Cosmic Noon, which were only known through a handful of ground-based observations of UV-bright or far-infrared-bright galaxies (e.g. P. L. Capak et al. 2015; J. Matthee et al. 2015; D. P. Stark et al. 2015; A. K. Inoue et al. 2016; S. Carniani et al. 2017). A number of *JWST* works have uncovered the increased scatter about the metallicity relations at $z > 4$ (e.g. K. Nakajima et al. 2023; M. Curti et al. 2024), including the possible breakdown of these fundamental relations (M. Curti et al. 2023, 2024).

We measured gas-phase metallicities adopting the strong-line calibrations for the high-z Universe presented in E. Cataldi et al.

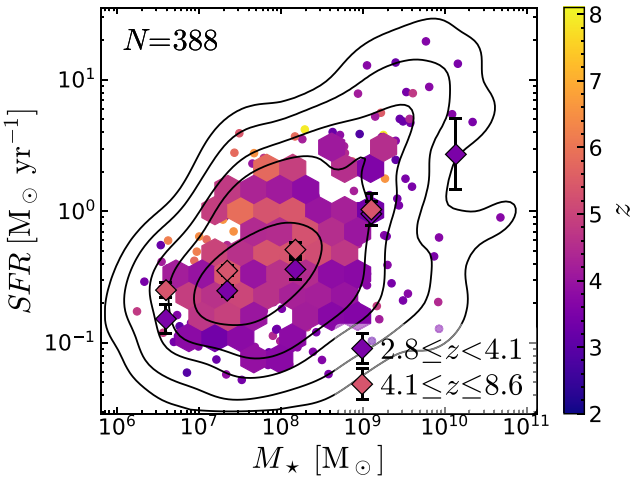

Figure 13. Redshift-collapsed star-forming main sequence from Dark Horse, at $z = 2.8$-8.6. Based on PROSPECTOR-derived $M_\star$ and on SFR from Dark Horse emission lines. The binned measurements highlight the increasing main-sequence zero-point at earlier epochs.

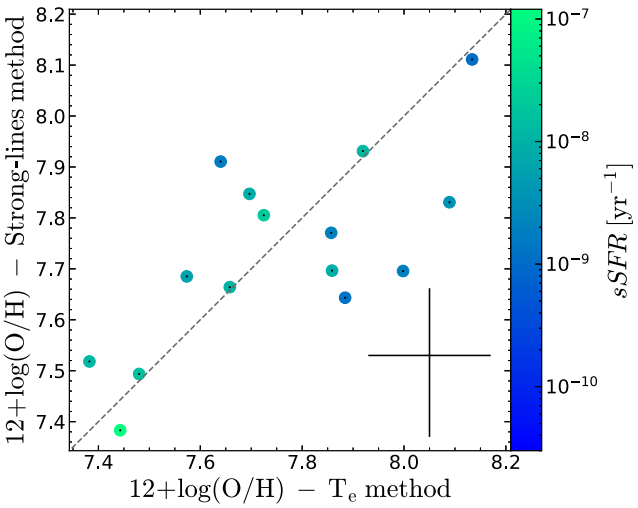

Figure 14. Comparison of gas metallicities between the direct T_e method and the strong-line method, colour-coded by specific SFR. Dark Horse measures 18 T_e-based metallicities (we removed four AGN with T_e-based metallicities). With these numbers, one can start analysing secondary correlations, underscoring the advantage of dense-shutter spectroscopy in gathering large samples of faint emission-line measurements. The cross represents the median errorbar, including the uncertainties on T_e.

(2025).[1] The strong-line metallicities are based on the dust-corrected strong emission-line ratios

$$R_3 \equiv \frac{[O\,\text{III}]\lambda 5007}{\text{H}\,\beta}$$

$$R_2 \equiv \frac{[O\,\text{II}]\lambda\lambda 3726, 3729}{\text{H}\,\beta}$$

$$\tilde{R} \equiv 0.88 \times \log_{10}(R_3) + 0.46 \times \log_{10}(R_2)$$

$$\text{Ne}_3\text{O}_2 \equiv \frac{[Ne\,\text{III}]\lambda 3869}{[O\,\text{II}]\lambda\lambda 3726, 3729}. \quad (3)$$

The best-fitting metallicity is found adopting a minimization approach as described in M. Curti et al. (2024), and an Markov Chain Monte Carlo (MCMC) [with D. Foreman-Mackey et al. (2013) implementation] is run to infer the uncertainties. In order to include a given diagnostic in the procedure, we request 3-σ detections on the involved emission lines, while upper limits on [O II]$\lambda\lambda$3726, 3729 and/or [N II]λ6583 are used to discriminate among the lower- and upper-metallicity branch in case R_3 is the only diagnostic available. This procedure allocates 354 strong-line metallicity measurements, roughly 10 times more than PID 1210, when considering only the 36 galaxies with grating measurements; for a fair comparison, we removed the prism-based metallicities (M. Curti et al. 2024), which in PID 1210 rely on 3× longer NIRSpec integration using the prism (A. J. Bunker et al. 2024).

In addition, we could apply the 'direct' T_e-based method (e.g. I. H. Laseter et al. 2024) for 18 galaxies with [O III]λ4363 auroral line detection at >3-σ significance, highlighting the potential of the Dark Horse approach in performing a less-biased search of this line emission in large galaxy samples (Fig. 14). When compared to strong-lines-based metallicities for the same galaxies, T_e-based metallicities are ∼0.07 dex larger on average (mean offset), with a scatter between the two measurements of ∼0.13 dex, consistent with the measurement uncertainties (the uncertainties on the T_e-based metallicity take into account also the uncertainties on T_e itself).

[1]See also R. L. Sanders et al. (2025) for recent developments.

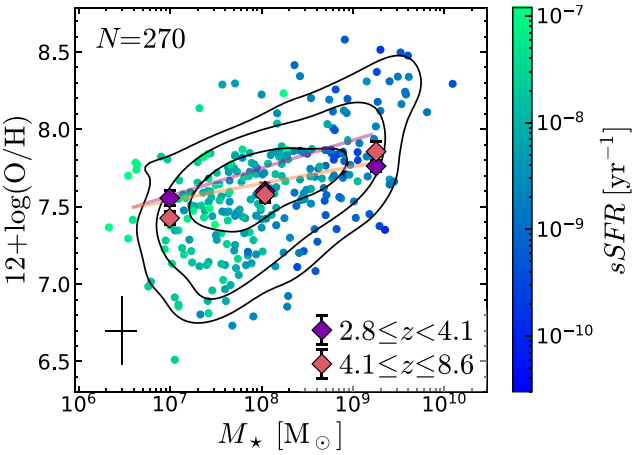

Figure 15. Mass–metallicity relation based on strong-line calibrations, illustrating the redshift evolution (using two equal-size subsets split by redshift), and the selection bias with star-forming activity (highlighted by the clear trend in sSFR). The horizontal lines are fits from M. Curti et al. (2024). The offset with respect to our measurement reflects the different strong-line calibrations used here.

With these numbers, a single pointing in Dark Horse mode delivers sufficient galaxies to reconstruct the mass–metallicity relation at $z = 3$-8 (Fig. 15). As for the SFMS (Section 6.1), here too the analysis does benefit from straightforward selection criteria. The colour coding shows the prevalence of evolved systems (low-specific SFR, sSFR) at the high-mass end (blue hues) and starburst systems at low $M_\star$ (green). The Dark Horse observing strategy provides almost the same gratings depth as deep pointings, but with sufficient flexibility to simultaneously probe $M_\star \lesssim 10^{10}$ M$_\odot$.

6.3 Probing CGM dust using background galaxies

The high-target density of Dark Horse and the depth of our observations enable using background galaxies to trace the CGM around massive galaxies. We report the case study of the sub-mm galaxy ALESS010.1 at $z = 3.471$ (Fig. 16; source 645 014 in Dark Horse). The background galaxy 634005 is red and compact and the photometry indicates a clear spectral break in F200W. If interpreted as a Ly α break, this would place 634005 at $z \gtrsim 16$. However, at this redshift, the rest-frame UV slope would be unusually flat ($\beta_{\rm UV} > 0$), and the stellar mass of the galaxy would be unusually large. SED fitting with PROSPECTOR finds $z_{\rm phot} = 16.4 \pm 0.5$ and $\log(M_\star/{\rm M}_\odot) = 9.3 \pm 0.3$ (see Section 6.5 for our PROSPECTOR setup). However, thanks to the depth of Dark Horse, we detect unambiguous H α emission at $z = 4.29$ (Fig. 16c), consistent with EAZY's secondary low-redshift solution, where the spectral break is the Balmer break, made stronger by dust attenuation.

However, even this low-redshift solution seems at first unlikely: In this case, the SED model infers a quiescent solution, with $\log(M_\star/{\rm M}_\odot) = 8.7 \pm 0.2$ and $A_{\rm V} \approx 1.4$ mag in the stellar continuum. Since dust attenuation correlates with $M_\star$ (e.g. L. Sandles et al. 2024; C. Woodrum et al. 2025), such a high amount of obscuration in such a low-mass galaxy seems unlikely – particularly for the stellar continuum. Intriguingly, other galaxies around ALESS010.1 also display unusual levels of attenuation, given their redshift and stellar mass. This suggests that the dust attenuation is in the foreground, such that these low-mass galaxies are probing dust in the CGM around the ALESS010.1, at distances of ≈20 kpc. This is smaller but comparable to the scales over which we see filamentary ionized structures – likely outflows – in quasar–submm galaxy pairs (100 kpc; B. Peng et al. 2025). An in-depth analysis has been presented in (F. Sun et al. 2026), but here we remark that Dark Horse spectroscopy provides a compelling way to use faint emission-line galaxies as a probe of diffuse CGM dust and, therefore, feedback mechanisms in massive galaxies.

6.4 Outflows

JWST enabled the study of energy and momentum injection from star formation and accretion at lower $M_\star$ than what was possible before (S. Carniani et al. 2024; R. A. Cooper et al. 2025; Y. Xu et al. 2025). Among the unexpected discoveries is the high-incidence rate of neutral-gas outflows, traced primarily by Na Iλλ5890, 5896 seen in absorption (S. Belli et al. 2024; F. D'Eugenio et al. 2024; R. L. Davies et al. 2024; E. Taylor et al. 2024; F. Valentino et al. 2025; P.-F. Wu 2025). These outflows seem to have much higher mass loading than the ionized phase (e.g. S. Belli et al. 2024; F. D'Eugenio et al. 2024). Crucially, they are seen also in quiescent galaxies, including old systems (Y. Sun et al. 2026), suggesting a role in keeping these galaxies from forming new stars.

In Dark Horse, we report the discovery of multiphase gas outflows in ID 175773 at $z = 2.54$. This dusty galaxy was selected with weight 10 (i.e. overriding the 300 nJy threshold from Section 2). It hosts an AGN identified via a tentative broad H α component (Section 6.6) and J. A. Baldwin, M. M. Phillips & R. Terlevich (1981; BPT) classification. Narrow-line detections include hydrogen recombination lines H β, H α, Pa δ, Pa γ, and Pa β. The forbidden lines [O III]λλ4959, 5007 and [S III]λλ9069, 9532 show a blueshifted wing, confirming the presence of out-

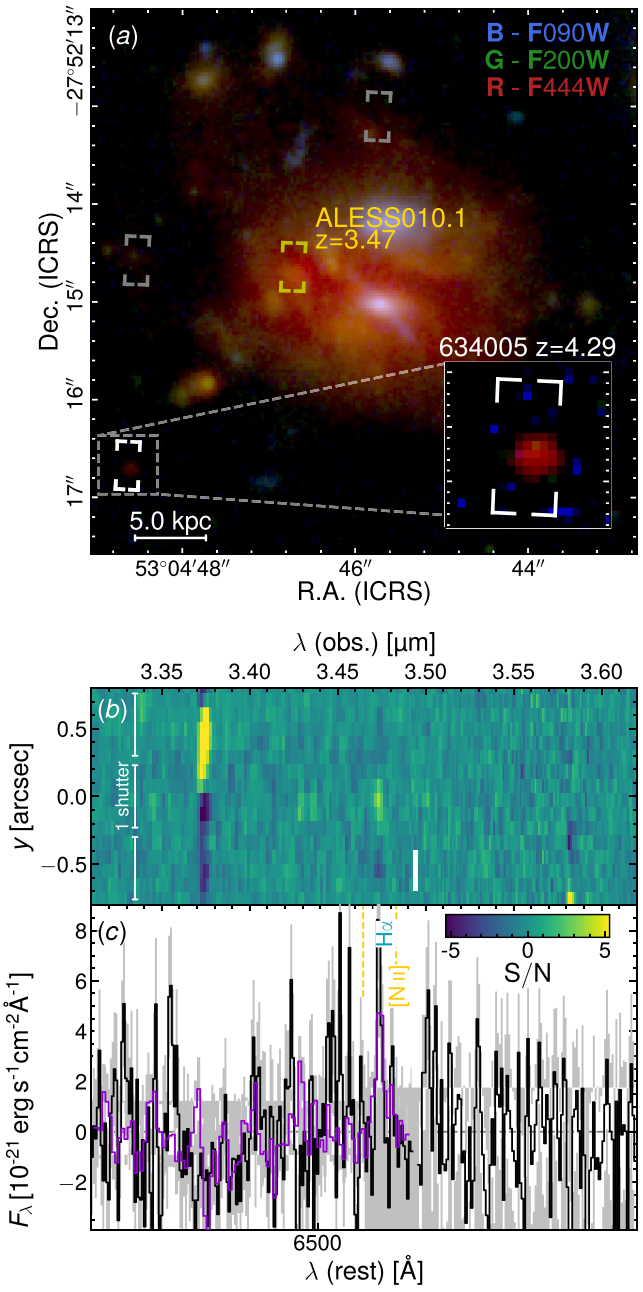

Figure 16. NIRCam false-colour image of the sub-mm galaxy ALESS010.1, which Dark Horse places at $z = 3.47$ (a). The bottom two panels show the grating spectra of the background galaxy 634005; the 2D SNR map from G395M (b) shows a clear detection in the centre of the shutter at $\lambda = 3.47$ μm, also seen in the negative images (the bright line at $\lambda = 3.37$ μm is a spectral overlap from a different shutter). The line at 3.47 μm is seen clearly in both the G395M and G235M 1D spectra (black and purple lines in panel c), ruling out an overlap. We identify this line with H α at $z = 4.29$ (matching [O III]λλ4959, 5007 is also seen in G235M, not shown here). By studying foreground dust extinction in background galaxies such as 634005, Dark Horse reveals the presence of dust in the CGM, at a distance of 20 kpc from ALESS010.1 (F. Sun et al. 2026). Grey shutters show Dark Horse targets without redshift.

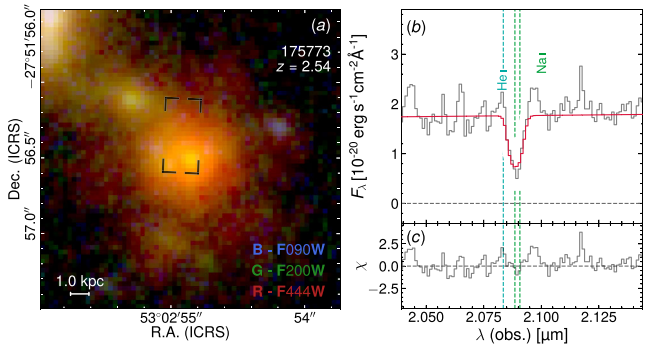

Figure 17. A dust-obscured AGN-host galaxy at $z = 2.5$ (ID 175773), displaying compact morphology and red colour in NIRCam (a). Dark Horse reveals deep Na Iλλ5890, 5896 absorption with a small (50 km s^{-1}) blueshift, tracing the galaxy ISM or a neutral-phase outflow (b and c). Dark Horse can take advantage of deep observations with high multiplex to also observe rare, bright sources for science cases that require long exposures.

flows previously detected using medium-band imaging (Y. Zhu et al. 2025, their source 209026).

We detect clear absorption near Na Iλλ5890, 5896, blueshifted by 50 km s^{-1}. Our model follows the approach of D. S. Rupke, S. Veilleux & D. B. Sanders (2005, see also R. L. Davies et al. 2024; J. Scholtz et al. 2024; P. G. Pérez-González et al. 2025). The model parameters are inferred in a Bayesian framework, using MCMC integration, to fully explore the degeneracies between correlated parameters (e.g. covering factor C_f and sodium optical depth at line centre, τ_0 Na Iλ5896, R. L. Davies et al. 2024). The resulting fiducial model is shown in Fig. 17. Using the geometry, metallicity, and ionization assumptions of Y. Sun et al. (2026), we estimate a mass outflow rate of $\log(\dot{M}_{\rm out}/({\rm M}_\odot\ {\rm yr}^{-1})) = 2.0 \pm 0.2$. As a reference, the maximal SFR (assuming no AGN contribution to the narrow component of H α) is $\log({\rm SFR}/({\rm M}_\odot\ {\rm yr}^{-1})) = 0.8 \pm 0.4$. So the mass loading factor is clearly above unity, confirming that neutral-phase outflows are capable of shutting down star formation (S. Belli et al. 2024; F. D'Eugenio et al. 2024).

Overall, these results show the potential for Dark Horse 'hybrid' surveys. Whenever the science goals require deep spectroscopy of sources with low on-sky density – and provided multi-band NIRCam coverage is available – any remaining detector real estate can be allocated to overlapping faint-source spectroscopy.

6.5 Mini-quenched galaxies

In addition to exploring faint and rare emission-line objects, the survey speed and depth of Dark Horse enable compelling non-detection science. Thanks to the combination of stringent upper limits on strong lines with the continuum shape from deep NIRCam photometry, Dark Horse enables to study star-formation burstiness which much higher precision than what is possible from photometry alone – even when using joint constraints from medium- and wide-band observations (e.g. S. Tacchella et al. 2022; C. Simmonds et al. 2025).

These improved constraints from fitting simultaneously photometry and spectroscopy can be used to study the stochasticity of SFR at high redshifts. Deep prism observations have shown the existence of low-mass galaxies ($M_\star \lesssim 10^9\ {\rm M}_\odot$) with negligible SFR (V. Strait et al. 2023; T. J. Looser et al. 2024; W. M. Baker et al. 2025). This population of 'miniquenched' galaxies are usually identified by their Balmer breaks (e.g. A. Kuruvanthodi et al. 2024; A. Covelo-Paz et al. 2026), lack of emission lines, and UV slopes $\beta_{\rm UV} \sim -2$, indicating lack of current star formation but very young light-weighted age. Their number abundance and physical properties hold compelling constraints on the duty cycle of star formation and on the time-scale and efficiency of feedback (D. Ceverino, R. S. Klessen & S. C. O. Glover 2018; C. C. Lovell et al. 2023; T. Dome et al. 2024, 2025; V. Gelli et al. 2024, 2025; W. McClymont et al. 2025; J. A. A. Trussler et al. 2025). The rapid cessation of star formation in these systems seems to require stronger or more efficient feedback than just supernovae (V. Gelli et al. 2024), and may point to bright quenched phases with little or no dust (W. M. Baker et al. 2025; A. Ferrara, A. Pallottini & L. Sommovigo 2025). While deep, medium-band photometry can identify 'lulling' or 'smouldering' galaxies (J. A. A. Trussler et al. 2025), direct spectroscopic constraints provide better time resolution than photometry alone, due to ∼100× narrower effective bandwidth. The price to pay, of course, is completeness, which Dark Horse spectroscopy mitigates substantially.

To illustrate the improved sensitivity in the low-SFR regime, we report the identification of a mini-quenched galaxy, ID 61416 at $z_{\rm phot} = 9.6$ (Fig. 18). We use photometry from the upcoming JADES Data Release 5 (B. D. Johnson et al. 2026; B. E. Robertson et al. 2026), and we compare the star formation histories obtained by fitting the photometry alone (indicated by the green lines and symbols in Fig. 18) versus a joint fit of the same photometry plus the Dark Horse spectrum (purple lines and symbols in Fig. 18). We use the Bayesian SED tool PROSPECTOR (B. D. Johnson et al. 2021), with the same setup as F. D'Eugenio et al. (2026). Specifically, we use a rising star-formation history (SFH) prior, inspired by the success of models of fixed baryon-conversion efficiency (e.g. S. Tacchella et al. 2018), and implemented as described in C. Turner et al. (2025, the rising prior is shown in grey, Fig. 18d). We use a flexible dust-attenuation law (S. Noll et al. 2009; M. Kriek & C. Conroy 2013), with extra attenuation for stars younger than 10 Myr, representing dust in birth clouds (S. Charlot & S. M. Fall 2000). The redshift is free to vary, with a Gaussian prior set by the EAZY photometric redshift, and truncated between $7.5 \leq z \leq 11$, dictated by the photometric drops seen in NIRCam. The photometry and Dark Horse G395M spectrum are shown in Fig. 18(a). We optimize the model twice: once based on photometry only (green lines and circles in Fig. 18), and once based on joint modelling of the photometry and Dark Horse spectroscopy (purple). The fiducial (maximum a posteriori) models are shown in Fig. 18(a), with the residuals in Fig. 18(b). The redshift of the source is strongly constrained by the non-detection in *F115W*; the photometry-only model interprets the moderate *F410M* photometric excess as strong [O II]λλ3726, 3729 emission, which should be detectable by NIRSpec. Lacking such detection in our data (grey spectrum in Fig. 18a), the spectrophotometric model revises the solution to an even lower recent SFR, suggesting that this galaxy is a 'mini-quenched' system, possibly the highest-redshift such system (V. Strait et al. 2023; T. J. Looser et al. 2024; W. M. Baker et al. 2025). The blue UV slope and extremely low-dust attenuation (Fig. 18c) make 61416 an excellent candidate for a 'blue monster' (F. Ziparo et al. 2023; A. Ferrara et al. 2025).

6.6 Broad-line AGNs

The Pilot Survey observed eight broad-line AGN (and one additional tentative source), of which seven were targeted (MSA weight 10; Table 2), and two were weight 1. Upon inspection of

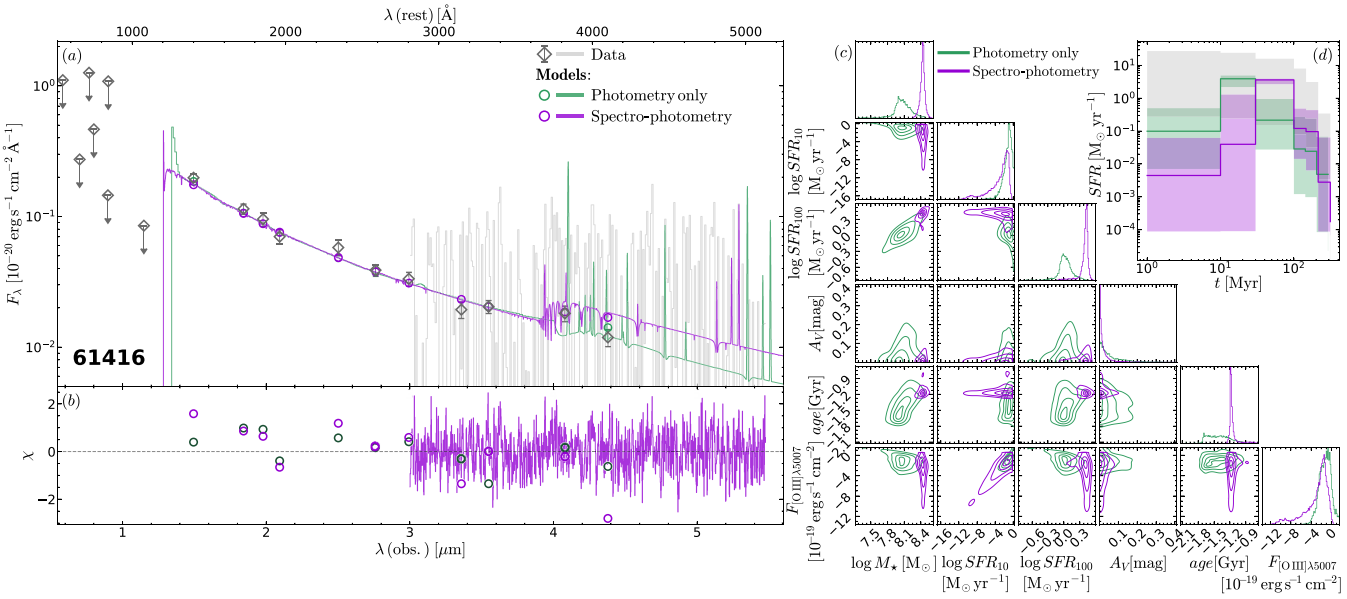

Figure 18. Including spectra from Dark Horse-undetected sources like 61416 at $z_{\rm phot} = 9.6$ can significantly impact the resulting SED model. The green lines and circles show the fiducial PROSPECTOR model based on NIRCam photometry only, whereas the purple lines and circles are the model based on joint fitting of NIRCam and the NIRSpec G395M spectrum from the Pilot Survey. The photometry-only model predicts bright [O II]λλ3726, 3729 that should be detectable by NIRSpec; therefore, including the observed spectrum rules out this solution and forces PROSPECTOR to seek a lower-SFR model, revealing 61416 as a 'mini-quenched' galaxy (similar to T. J. Looser et al. 2024; W. M. Baker et al. 2025).

Table 2. Summary of broad-line AGNs (including LRDs) in Dark Horse.

ID	R.A.	Dec.	Weight	$z_{\rm phot}$[a]	$z_{\rm spec}$	LRD
175773[b]	53.048578	−27.865698	10	6.02	2.5486 ± 0.0001	0
5756	53.062410	−27.901838	10	3.72	3.437 25 ± 0.000 03	1
171973[c]	53.086836	−27.873046	10	5.43	3.4715 ± 0.0002	0
13064	53.102832	−27.890974	1	3.67	3.563 35 ± 0.000 02	1
160128	53.050301	−27.900055	10	4.73	3.614 01 ± 0.000 02	1
5070	53.092004	−27.903136	10	3.62	3.643 72 ± 0.000 02	1
35 453	53.057029	−27.874376	10	5.06	3.659 81 ± 0.000 01	1
634042	53.064113	−27.870934	10	6.05	5.5359 ± 0.0005	1
642396	53.095910	−27.906901	1	5.83	6.5535 ± 0.0002	1

Note. Objects with 'LRD' flag 1 have a V-shaped SED in NIRCam.
[a]We show photometric redshifts from the internal catalogue v0.9.5 RC2.
[b]Tentative broad line; classified as type 2 AGN using the BPT diagram (J. A. Baldwin, M. M. Phillips & R. Terlevich 1981).
[c]X-ray emitter, see also D. D. Kocevski et al. (2025).

their NIRCam SED, two AGN (175773 and 171973) show weak UV emission (as expected from dust reddening) while the spectra show clear [N II] emission; they appear to be dust-obscured AGN (171793 is also an X-ray emitter; D. D. Kocevski et al. 2025). The other seven display the V-shaped SED typical of LRDs (J. Matthee et al. 2024; C. C. Williams et al. 2024). Thanks to its straightforward mask allocation with two priority classes, we can weight these detections by the inverse of the acceptance rates, which were 0.66 and 0.35 for weight 10 and weight 1, respectively (Section 2.2). The completeness-corrected number of broad-line AGN would then be ≈17.

With the depth of the grating observations, Dark Horse can measure accurate broad-line shapes, line fluxes, and even auroral line fluxes. Of course, the current limitation is the inability to measure accurate EWs, which would require forward modelling and removal of all overlapping sources.

To demonstrate the power of Dark Horse, we measure the narrow- and broad-line fluxes of the seven AGNs, with the same approach as outlined in F. D'Eugenio et al. (2025a, 2026). We mask prominent emission lines, then use a cubic spline to fit the continuum, with linear interpolation across masked regions. The narrow lines are modelled as Gaussians with common redshift and velocity dispersion; for doublets arising from the same upper level, we model the two lines using the flux of the brightest line as free parameter, and the the fixed flux ratio given by atomic physics, which we retrieve from PYNEB (V. Luridiana, C. Morisset & R. A. Shaw 2015). For any doublet arising from the same lower level ([O II]λλ3726, 3729 and [S II]λλ6716, 6731) the free parameters are the flux of the bluest line and the doublet flux ratio, with the latter constrained to the range allowed by atomic physics. We model only three narrow Balmer lines, H α, H β, and H γ, using fixed flux ratios appropriate for Case-B recombination, $T_{\rm e} = 10\,000$ K and $n_{\rm e} = 100$ cm^{-3}. The actual fluxes are then modulated using the G03 dust-extinction law, parametrized by the attenuation $A_{\rm V}$. For the LRDs, the broad lines are the sum of a Gaussian and an Gaussian convolved with an exponential

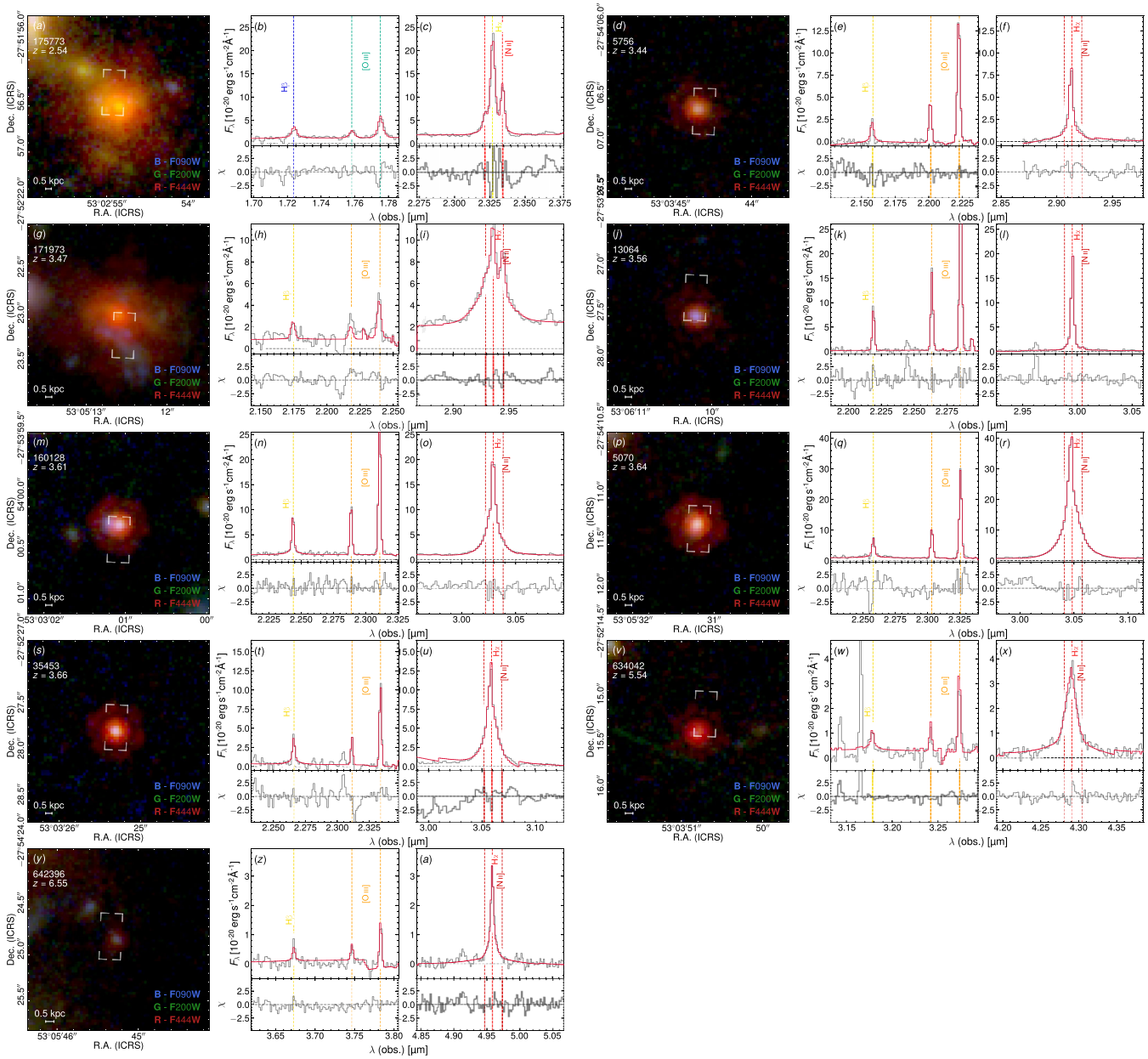

Figure 19. A collection of broad-line AGN (and candidates) in Dark Horse, including seven LRDs. For each target, we show the NIRCam RGB image, and the spectrum and fiducial model in the region of H β–[O III]$\lambda\lambda$4959, 5007 and H α-[N II]$\lambda\lambda$6548, 6583. dense-shutter can rapidly gather compelling samples of high-quality LRD spectra with broad spectral coverage, enabling the study of the broad-line profiles, absorbers, narrow-line properties, and photoionization diagnostics. We find a remarkable range of broad-line shapes and luminosities.

kernel, representing respectively direct light from the broad line, and light scattered by free electrons (V. Rusakov et al. 2026). The scattering process is parametrized by the optical depth τ_e and by T_e (see F. D'Eugenio et al. 2025a, for more details). Finally, we also model H α absorption, using the same approach outlined in I. Juodžbalis et al. (2024) and Section 6.4. A compilation of the broad-H α lines is shown in Fig. 19, highlighting the diversity of profile shapes, narrow-to-broad flux ratios, and [O III]λ5007/H β ratios.

6.7 Overdensities and clustering

Since the high spectroscopic completeness and efficiency of this programme are ideal for constructing spectroscopic redshift catalogues, this programme is also well suited for identifying high-redshift galaxy overdensities and performing clustering analyses. Given the improved sensitivity of NIRSpec/MSA when compared to NIRCam/WFSS, fainter galaxies can be identified, thereby probing galaxies that are nearly an order of magnitude less luminous than galaxies selected by NIRCam/WFSS at fixed survey time.

As a first look at the scientific prospects of using dense-shutter NIRSpec/MSA for overdensity identification and clustering anal-

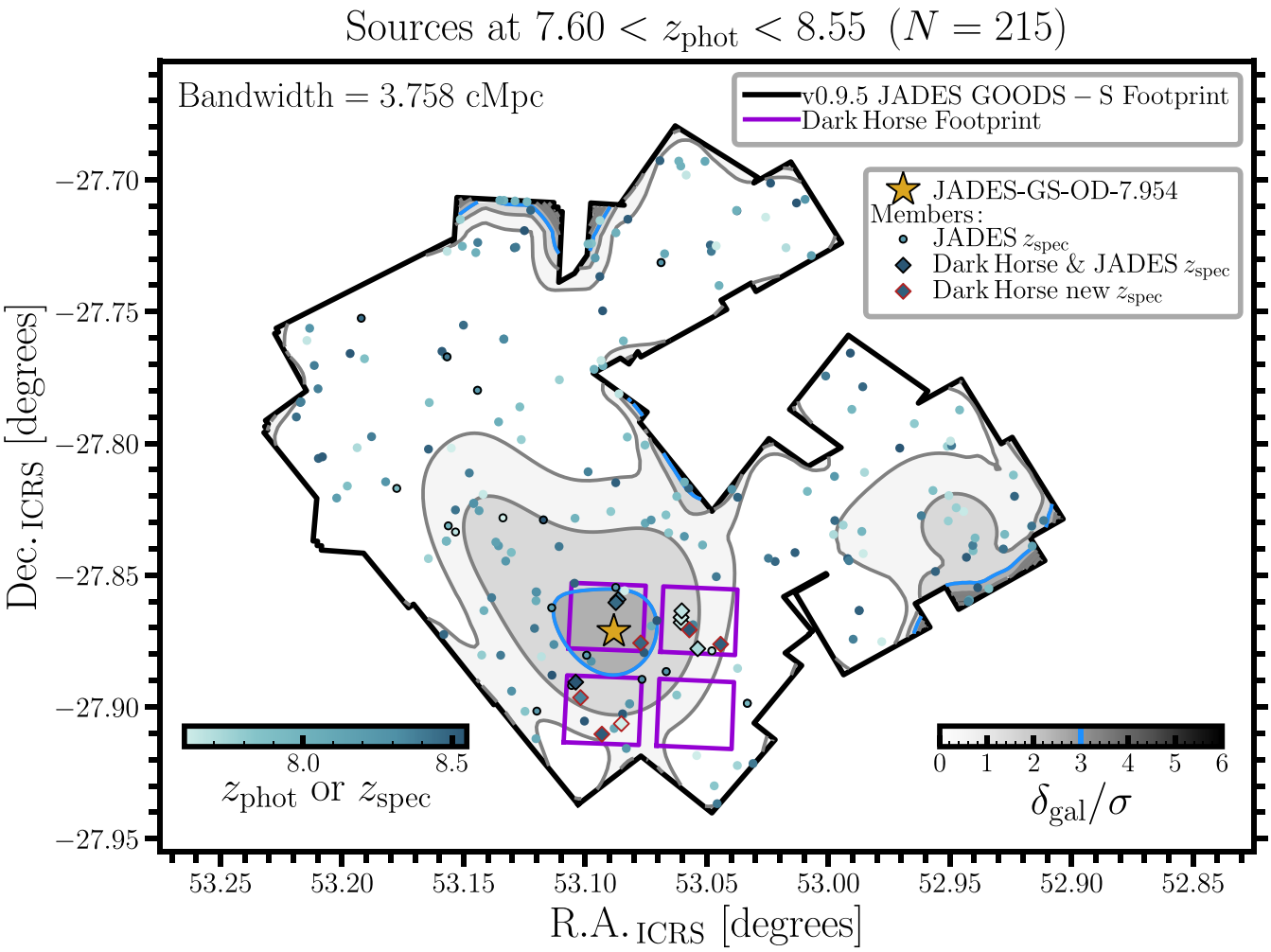

Figure 20. Dense-shutter NIRSpec/MSA is particularly well suited to study high-redshift galaxy environments by combining the improved completeness of slitless spectroscopy with the improved depth of slit spectroscopy. Here we show the spatial distribution of $N = 215$ galaxy candidates at $7.60 < z_{\rm phot} < 8.55$ from the JADES photometric sample, colour-coded by their photometric redshift, or spectroscopic redshift, if available. The thick black polygon represents the JADES/NIRCam GOODS-S footprint. The underlying density field of the photometric sample is determined using a KDE, following the methodology from J. M. Helton et al. (2024) and F. D'Eugenio et al. (2025c). The contours illustrate the estimated density field and the blue contours represent a significance level of 3σ. Aside from the $>3\,\sigma$ peaks near the boundary of the footprint, which are the result of edge effects, the only other significant peak is spatially coincident with a spectroscopically confirmed galaxy overdensity at $z = 7.954$ (JADES-GS-OD-7.954; J. M. Helton et al. 2024), as shown by the gold star. The Dark Horse single MSA pointing (purple outline) identifies 13 spectroscopically confirmed members of this overdensity (diamonds with black outlines), including six new members (diamonds with red outlines).

ysis, we search for new members of an extreme galaxy overdensity at $z \approx 8$ identified by J. M. Helton et al. (2024), JADES-GS-OD-7.954, which is the third highest redshift spectroscopically confirmed galaxy overdensity to date. The location of JADES-GS-OD-7.954 is illustrated by the gold star in Fig. 20 and falls within the Dark Horse Pilot Survey pointing. This protocluster candidate originally contained four galaxies identified with NIRCam/WFSS from FRESCO (First Reionization Epoch Spectroscopically Complete Observations; P. Oesch, 2024) and represented a density around ∼6 times that of a random volume. Fig. 20 also shows the spatial distribution of $N = 215$ galaxy candidates at $z \approx 8$ from the JADES photometric sample to further demonstrate the significance of the overdensity JADES-GS-OD-7.954 (including six Lyα emitters; G. C. Jones et al. 2025). Following the methodology described in F. D'Eugenio et al. (2025c), we determine the underlying density field of the photometric sample by using a kernel density estimator (KDE). To quickly summarize, we assumed Gaussian kernels for the KDE and optimized the bandwidth (also known as the smoothing scale, as shown in the upper left corner of Fig. 20) by maximizing the likelihood cross-validation quantity. The estimated density field is illustrated by the contours, where purple contours represent overdensities above a significance level of 3σ. The only significant peak not affected by edge effects is spatially coincident with JADES-GS-OD-7.954.

It is obvious from looking at the upper panel of Fig. 9 that there is an abundance of galaxies at $z \approx 8$. Indeed, 13/29 galaxies at $z > 7$ are within $\Delta z = 0.1$ of JADES-GS-OD-7.954, demonstrating the importance of cosmic variance when selecting samples of the highest redshift galaxies. Out of these 13 galaxies, six are new discoveries, demonstrating the efficacy of using dense-shutter NIRSpec/MSA for identifying faint populations of clustered galaxies. Future work should look into identifying overdensities and voids

with dense-shutter NIRSpec/MSA, especially given the recent discovery of pristine massive star formation caught at the break of cosmic dawn with NIRCam/WFSS in Abell 2744 (T. Morishita et al. 2025).

7 DISCUSSION

7.1 Dark Horse relative to slitless spectroscopy

Having now presented the results of this programme, we turn to some more detailed aspects of the trade-off relative to the *JWST* slitless grism modes. We stress that while we see considerable advantages of the dense-shutter method, there are also ways in which the grism might be preferred, such that each method has preferred applications.

7.1.1 Emission-line sensitivity

To assess the dense-shutter method relative to slitless, we start with a comparison of their emission line sensitivities (Fig. 21), comparing to the deep NIRCam/WFSS observations from *JWST* Cycle-3 PID 4540 (D. J. Eisenstein et al. 2025; F. Sun et al. 2026.). This programme used the *F322W*, *F356W,* and *F444W* filters and GRISMC to obtain grism spectroscopy of galaxies in the JOF across 2.4–5.0 μm, and the total grism exposure time is 82 ks, comparable to that of Dark Horse (69.4 ks). PID 4540 uses a 2×2 mosaics of NIRCam pointing, and therefore the median integration time is ≈3-5.4 h in each of the three bands. Improving the grism sensitivity to 10-h on-source equivalent (matching the on-source time of Dark Horse), the difference of depth between NIRCam/WFSS and Dark Horse is a factor of ≈3 (Fig. 21a). Of course, this would require at least a 2.5 longer survey with NIRCam, given the actual survey times.

In contrast, in Fig. 21(b), we show a comparison of the *actual* sensitivities, achieved at almost equal on-source time (actually, slightly longer for NIRCam). The median 5-σ emission-line sensitivity of PID 4540 for unresolved lines is ≈5 times of that for Dark Horse across 3.3–5 μm, a factor of 25 in integration time. The sensitivity improvement is even larger at shorter wavelengths, exceeding a factor of 10 (100 in integration) at $\lambda < 3$ μm.

This comparison highlights the high efficiency of the dense-shutter approach in obtaining deep emission-line spectroscopy of a large sample of high-redshift galaxies. We also note that preliminary analyses of PID 4540 (F. Sun et al. 2026) yield ≈50 per cent more redshifts at $z > 3$ than Dark Horse. This is a result of the higher completeness with slitless spectroscopy and the flux density cap employed for Dark Horse.

7.1.2 Geometry, field of view, and completeness

When it comes to survey speed, the instrument field of view matters. The total footprint of the four MSA quadrants of NIRSpec is about 9.82 arcmin^2, similar to the NIRCam field of view (9.30 arcmin^2) and about twice that of NIRISS. It is important to note that the relatively high-resolution of the NIRCam grism means that the spectral traces are long and hence the coverage at any given wavelength is often limited by the field stop, reducing the field of view. In contrast, with the MSA gratings, one obtains the full wavelength coverage per target, save the small detector gap. However, single-configuration completeness greatly reduces the effective footprint of the MSA, even when allowing spectral overlaps. Since NIRSpec picks from a catalogue, the actual penalty

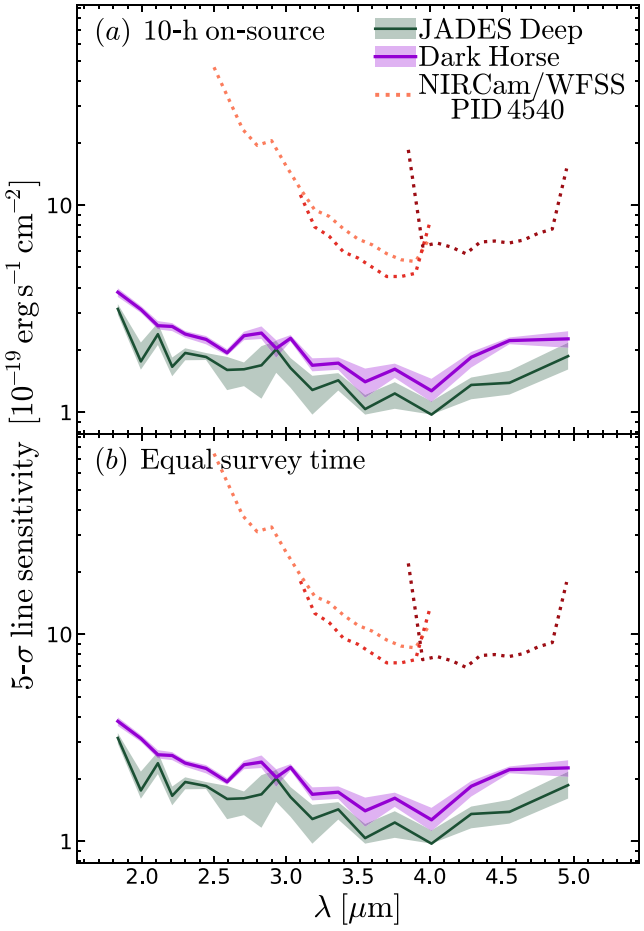

Figure 21. A comparison between dense-shutter spectroscopy and NIRCam/WFSS. The purple and green lines are the same as in Fig. 6, where we use nod background subtraction (while master background would deliver even better sensitivity). The red dotted lines show the median NIRCam/WFSS 5-σ sensitivity with PID4540 in the *F322W2*, *F356W*, and *F444W* band (3–5.4-h exposures; D. J. Eisenstein et al. 2025; F. Sun et al. 2026). In panel (a), we scale the sensitivity of NIRCam/WFSS to the same on-source time as NIRSpec/MSA, while panel (b) shows the actual measured values, which correspond to approximately the same survey time. Note that NIRCam/WFSS delivers 50 per cent more sources with $z > 3$ than dense-shutter.

depends on the target density of the parent sample (Section 7.2). Here, we use the completeness of Dark Horse to evaluate the method, i.e. 854 out of 2516 allocated targets, or 35 per cent (Section 2.3). The dominant factors are MSA slit vignetting (0.64 with our choice of `entire_open`) and the three-shutter requirement (0.60), with a smaller penalty due to exclusion zone in the dispersion direction (0.9). Thus the effective MSA footprint is 9.82 arcmin^2 × 0.64 × 0.60 × 0.9 ≈ 3.4 arcmin^2, which we will use below. If high completeness in a given field is needed, one could use multiple MSA configurations offset by a half-integer or even third-integer shutter spacing to access most targets. Alternatively, increasing the number of allowed overlaps can also be achieved, both in the spatial direction (by moving from 3-shutter to 2- or 1-shutter slitlets) and/or in the spatial direction (by overriding MPT minimum target separation of 4 shutters). We note that slitless spectroscopy does not immediately yield full completeness either, because of overlap with brighter sources; one needs to use multiple dispersion angles.

Operationally, slitless spectroscopy does not require pre-imaging for target selection, although such imaging may be desired for line association and for the science application. It is the only option for pure parallel observing, and observations allowing many mechanism moves can produce compelling data sets of both imaging and spectroscopy in novel fields (e.g. F. Sun et al. 2025). Further, it can be awkward that the NIRSpec footprint of four quadrants in a near square is rather different than the NIRCam footprint: One not only needs pre-imaging for dense-shutter to be possible, but typically one needs a filled mosaic of at least 2×2 pointings if one is to cover the 3.1 × 3.4 arcmin^2 bounding box of the NIRSpec MSA.

7.1.3 Sensitivity, bandwidth, and survey speed

As expected, strong suppression of the background by the MSA and the larger pixels of NIRSpec (0.1 arcsec compared to 0.06 arcsec in NIRCam LW and NIRISS) sharply suppresses noise. Comparing to PID 4540, which represents a 20 per cent longer time investment than Dark Horse, dense-shutter delivers a 4–10-fold improvement in line sensitivities above NIRCam, depending on wavelength (Fig. 21). This is nominally a factor of 16–100 advantage in exposure time. We note that this result is still using nod-based same-pixel background subtraction; we expect that the data could also be reduced with non-local modelling, or 'master background' subtraction, which would suppress the noise further and avoid self-subtraction within larger galaxies. This would make the case for single-shutter configurations even more compelling. Indeed, one could measure accurate line fluxes without performing any background subtraction at the pipeline level, as demonstrated in Fig. 12, showing that – at least for emission-line science which is most relevant here – *single-shutter configurations are both feasible and less noisy, even without master background.*

But further, the instantaneous bandwidth of NIRSpec is wider. The G395M grating alone covers 2.9–5.3 μm, even more than the union of the NIRCam *F356W* and *F444W* filters. If one wants full wavelength coverage, this is another factor of 2 over the grism. Of course, NIRSpec also offers the G140M and G235M gratings. Using all three would give spectra from 0.7 to 5.3 μm. Importantly, NIRISS only goes as red as 2.2 μm, while the NIRCam grism has a zero-dispersion wavelength of 3.95 μm and hence a sharply reduced field of view (and reduced first-order throughput) shortward of 3 μm, ending at 2.4 μm. This strongly favours the use of G235M to cover the 2–3 μm wavelength range; notably this disperser will capture the strong H α or [O III]λ5007 lines for $1.6 < z < 5.3$, which is a workhorse range for galaxy evolution studies with *JWST*, capturing the epoch when ∼50 per cent of the stellar mass in the Universe formed (e.g. P. Madau & M. Dickinson 2014), and the emergence of low-mass, environment-quenched galaxies (M. Donnari et al. 2021a, b).

To place these considerations on a more quantitative footing, we consider as a figure of merit the integral over wavelength of area times inverse variance (5-σ point source), per unit time. For the NIRCam grism, we use data from the pure-parallel programme SAPPHIRES (Slitless Areal Pure Parallel HIgh-Redshift Emission Survey, PID 6434, PI E. Egami; Sun et al. 2025, their table 2). Adopting units of (arcmin^2) $(\times 10^{-18}$erg s^{-1} cm$^{-2})^{-2}$ (μm ks^{-1}), and assuming $\Delta\lambda = 0.2$ μm, we obtain metrics of 0.653, 0.677, 0.585, and 0.638 for 356W R, F356W C, F444W R, F444W C, respectively (i.e. around 0.64 on average). This includes an average correction to take into account 20 per cent more noise in module B than module A.

For Dark Horse, we consider the effective MSA quadrant area of 3.4 arcmin^2, as described in Section 7.1.2. For G395M, we integrate the sensitivity curve (Fig. 6) and obtain a metric of 7.5, roughly ten times higher than NIRCam. This suggests that the dense-shutter method is ten times more efficient than doing both *F356W* and *F444W* with the grism.

To summarize, the key argument for the dense-shutter mode is that the improvements in line sensitivity, field of view, and wavelength coverage far outweigh the factor of ∼2–3 reduction of single-configuration completeness.

7.1.4 Caveats

Here we discuss some specific scenarios, and considerations that are difficult to quantify and may depend on the specific application. While NIRSpec delivers nearly the full wavelength range on all objects, save the detector gap, grism slitless spectroscopy yields a complex distribution of wavelength coverage across the field, which does not enter our metric. While the proposed metric is useful for the question of finding a single bright line in as many objects as possible, if one cares only about a single wavelength, the grism could switch to a medium-band filter, boosting inverse variance by a factor of 2.5. In this case, the useable field of view would also be larger; for example, F410M could get a metric of around 2.5, comparable to dense-shutter (i.e. 7.5). On the other hand, the proposed metric does not capture the requirement to have coverage of two well-separated lines. The grism loses further efficiency here, unless one is tiling fairly big areas. Of course, the reported advantage of G395M becomes even stronger in G235M, because the grism area and throughput drops badly shortward of 3 μm.

But there are arguments and opportunities for the grism modes as well. To start, the grism modes can have lower operational overheads. In particular, if one only needs relatively shallow line sensitivities, short exposures with the grisms may suffice, plus one is getting nearly full targeting completeness in one exposure. There is no value in taking NIRSpec exposures shorter than about 500 s, as the detector noise and MSA overheads will be severe. We note that at this time, *JWST* operations require direct images when NIRCam and NIRISS are used as the prime instrument; these do add overheads not dissimilar to the MSA target acquisition sequence. Having high single-exposure completeness is particularly useful for applications like surveys of quasar environments (e.g. D. Kashino et al. 2023; F. Wang et al. 2023): here one is primarily interested in a known wavelength and a small neighbourhood around the quasar, blunting some of the advantages of MSA spectroscopy.

Slitless spectroscopy is better for the study of line morphologies. Because of the complicated pattern of the MSA vignetting and the coarser NIRSpec pixel scale, extracting morphologies from MSA spectroscopy requires very careful modelling. We note that the combination of measuring the line with both a grism and a direct image can yield compelling dynamics studies (e.g. E. Nelson et al. 2024; A. L. Danhaive et al. 2025). In addition, slitless spectroscopy is also more reliable for the measurement of line fluxes, particularly from extended objects, because one is simply using photometric techniques in the dispersed images. Flux calibration through the MSA slits requires detailed modelling of the slit vignetting even for cases of known morphological profiles, and of course deviations from the assumed profiles cannot be corrected at all, as one has not measured the light beyond the slit.

7.2 Impact of sample selection

The figure of merit reported above depends linearly on the effective survey footprint, which in turn is linked to the completeness and to the characteristics of the input sample. The quoted completeness of 0.35 and effective area of 3.1 arcmin^2 are specific of design choices of Dark Horse, not of the dense-shutter method.

To start, the choice of 3-shutter slitlets imposes a loss of efficiency over single-shutter observations, because the fraction of operable shutters is 0.74, but the fraction of operable three-shutter slitlets is only 0.60. This means Dark Horse could have allocated ≈1100 targets with no loss in sensitivity (actually, with a modest gain, since we would open only 1100 shutters, against the actual 2562). This change of strategy would raise the completeness to 0.43. These numbers have been verified with MPT, but for the actual Dark Horse implementation we adopted a more conservative approach.

The value of 0.43 is close to the maximum efficiency ceiling; one could consider relaxing the shutter acceptance zone, but this would overly penalize compact sources, more so at short wavelengths, where the telescope PSF is smaller than the 0.2-arcsec bar shadows on the MSA. On the other hand, while we noted that Dark Horse operates in the regime where completeness is set by vignetting and shutter operability, this is directly linked to the target density ≈150-350 arcmin^{-2} in the two imaging areas. For instance, removing our redshift cut, we are left with 12 000 sources inside the four MSA quadrants, reaching target densities of 700–1700 arcmin^{-2}. Using a single shutter per source, MPT can allocate ∼5000 sources, but this exceeds the threshold where overlapping background is becoming the dominant noise source. In this case, to contain background noise (i.e. max 10 sources per row, Section 2.4), one would want to stay below $342 \times 10 \sim 3500$ sources, so the completeness would be $3500/12\,000 \approx 0.3$. On the other hand, additional gains are possible if one allows multiple visits; in this case, one could *reduce* the shutter acceptance area, which for each mask gives priority to sources with good slit centration and, therefore, higher throughput.

7.3 Other NIRSpec dispersers

We note that below 2 μm, the background increases again, rising to 45–60 nJy per NIRSpec pixel (applicable to JOF in December). Since the photon rate per frequency scales as λ^{-1}, the rise in background at short wavelengths causes a sharp rise in background noise, roughly 2× between 2 and 1 μm. With a background noise of 4 e$^-$, G140M suffers from a much stiffer noise penalty than the other two gratings, such that an overallocation of two sources would already cause the background noise to reach the detector noise. An overallocation of ≈7.5, as used here, would imply a time penalty of 3–4, erasing most of the advantage of dense-shutter over non-overlapping spectroscopy.

When considering the high-resolution gratings, the background is dispersed 3×, allowing the ceiling of 0.43 completeness to be reached even for the highest target densities. The trade-off here is spectral truncation at the red end of quadrants 1 and 2 of the MSA.

We next consider the trade-offs between using this dense-shutter approach with the grating method and using the NIRSpec prism dispersion mode. While the PRISM spectra should typically not be overlapped because they are background-limited and hence would increase the dominant noise source, the spectra are short enough that one can reach multiplex of nearly 200. Given that the PRISM covers the same wavelength range as the union of all three gratings, the difference in multiplex is only modest. However, per unit exposure time, the PRISM cannot achieve the line flux sensitivity of the gratings because the higher throughput of the prism cannot offset the increased noise from under-resolving the continuum and background. For the detection of emission lines, the gratings are likely to win this multiplexing assessment. A future analysis of overlapping prism spectroscopy will clarify the trade-offs.

Of course, achieving continuum spectroscopy even at modest SNR is scientifically important. This provides the detection of Lyman breaks, indeed a faster route to a redshift for UV-bright galaxies at $z > 9.5$ than the detection of rest-UV emission lines, and the measure of Balmer and 4000-Å breaks, important for the study of older stellar populations.

On the flip side, the PRISM under-resolves the emission lines. The gratings are needed to deblend certain close lines as well as to measure dynamics and outflows (Section 6.4). And as one gets fainter than 100 nJy, continuum detections require very long exposures, such that the emission lines provide much of the science. Indeed, the combination of grating redshifts and multi-colour NIRCam imaging can support modelling of the continuum shape, such as for Balmer breaks (Section 6.5). This is particularly relevant for young galaxies, where the continuum is dominated by young, hot stars or even nebular emission, which have low-EW features that are difficult to capture even with the prism.

8 SUMMARY AND CONCLUSIONS

In this article, we presented the Dark Horse spectroscopy survey using NIRSpec/MSA in 'dense-shutter' mode. Building upon the experience of previous studies that allowed moderate overlaps, Dark Horse allows for full spectral overlap on the NIRSpec detector, bridging the multiplex of slitless spectroscopy and the sensitivity of slit observations. To be effective, dense-shutter spectroscopy must build upon existing, pan-chromatic and spatially contiguous NIRCam imaging. For this survey, we leverage the JADES Origins Field (D. J. Eisenstein et al. 2025) and obtain a single pointing with G235M and G395M, focusing on $z > 3$ extragalactic science (Section 2). The existing deep NIRCam coverage in legacy extragalactic fields provides many opportunities for using dense-shutter spectroscopy.

After reducing the data using off-the-shelf methods, we confirm the feasibility of the method. Spectral overlaps cause additional background noise, which we do detect. With the adopted setup of Dark Horse, we predict a noise penalty of 1.30, corresponding to a time penalty of 1.7 to achieve the same sensitivity as standard MSA (Section 2.4). These numbers are confirmed experimentally (Section 3), meaning we are able to predict the MSA performance in Dark Horse, and use this knowledge for survey design. As we argue below, a time penalty of 1.7 is perfectly acceptable.

We find a redshift success rate of at least 0.65, comparable yet higher than grating surveys of similar depth (∼0.52). This result is likely driven by the high-quality photometric redshifts available in GOODS-S, and especially in JOF, where there is extensive and deep medium-band coverage. Nevertheless, an important component of the success rate could be the high completeness, which enables targeting compelling sources without having to resort to 'filler' targets.

What makes the dense-shutter spectroscopy worth it, of course, is the five-fold increase in survey speed relative to moderate-

overlap grating surveys (Section 4). To demonstrate the method – aside from measuring redshifts and line fluxes – we present several science applications of dense-shutter spectroscopy (Section 6). These range from classic studies of emission lines as probes of star formation (Section 6.1) and metallicity (Section 6.2), to studies of multiphase gas outflows (Section 6.4) and broad-line AGNs (Section 6.6). Sensitive, high-completeness observations also enable studies of CGM dust at $z \sim 3.5$ (Section 6.3), and even non-detections add value to existing photometry, by delivering informative flux upper limits that improve the constraints on photometric SFHs (Section 6.5).

Reviewing the above makes clear why the pursuit of a general-purpose spectroscopy of a high-density sample of faint galaxies in established *JWST* imaging fields is so well suited to this dense-shutter grating mode. These sources often have strong emission lines that are both efficient for redshift determination and essential for physical characterization. The density of sources is very high, enough to support the high multiplex of this MSA mode.

While our Dark Horse survey identified no unmitigatable problems, further optimizations are also possible, since there are trade-offs between different MSA configurations and targeting choices (Section 7). These future improvements could possibly make dense-shutter an even more compelling path to efficiently obtain large numbers of *JWST* spectra in deep cosmological fields, with depths that cannot be reached by the grism or by any current ground-based instrument.

ACKNOWLEDGEMENTS

We thank the anonymous referee for his insightful comments, which helped clarify and improve this article. This work is based on observations made with the NASA/ESA/CSA *James Webb Space Telescope*. The data were obtained from the Mikulski Archive for Space Telescopes at the Space Telescope Science Institute, which is operated by the Association of Universities for Research in Astronomy, Inc., under NASA contract NAS 5–03127 for *JWST*. These observations are associated with programme #3215.

FDE, RM, XJ, JS, IJ and GCJ acknowledge support by the Science and Technology Facilities Council (STFC), by the ERC through Advanced Grant 695671 'QUENCH', and by the UKRI Frontier Research grant RISEandFALL. DJE, CNAW, BDJ, BR, and ZJ acknowledge support from the NIRCam Science Team contract to the University of Arizona, NAS5-02015. DJE, JMH and BR also acknowledge support from *JWST* Programme 3215. Support for programme #3215 was provided by NASA through a grant from the Space Telescope Science Institute, which is operated by the Association of Universities for Research in Astronomy, Inc., under NASA contract NAS 5–03127. DJE was supported as a Simons Investigator. RM also acknowledges funding from a research professorship from the Royal Society. SC and EP acknowledge support by European Union's HE ERC Starting Grant No. 101040227 – WINGS. AJB, AJC and JC acknowledge funding from the 'FirstGalaxies' Advanced Grant from the European Research Council (ERC) under the European Union's Horizon 2020 research and innovation program (Grant agreement no. 789056). IJ also acknowledges support by the Huo Family Foundation through a P.C. Ho PhD Studentship. ST acknowledges support by the Royal Society Research Grant G125142. SA and MP acknowledges grant PID2021-127718NB-I00 funded by the Spanish Ministry of Science and Innovation/State Agency of Research (MICIN/AEI/ 10.13039/501100011033). MP also acknowledges the grant RYC2023-044853-I, funded by MICIU/AEI/10.13039/501100011033 and European Social Fund Plus (FSE +). EC-L acknowledges support of an STFC Webb Fellowship (ST/W001438/1). ALD thanks the University of Cambridge Harding Distinguished Postgraduate Scholars Programme and Technology Facilities Council (STFC) Center for Doctoral Training (CDT) in Data intensive science at the University of Cambridge (STFC grant number 2742605) for a PhD studentship. YI was supported by JSPS KAKENHI Grant No. 24KJ0202. The research of CCW was supported by NOIRLab, which is managed by the Association of Universities for Research in Astronomy (AURA) under a cooperative agreement with the National Science Foundation. JW gratefully acknowledges support from the Cosmic Dawn Center through the DAWN Fellowship. The Cosmic Dawn Center (DAWN) was funded by the Danish National Research Foundation under grant no. 140. The authors acknowledge use of the lux supercomputer at UC Santa Cruz, funded by NSF MRI grant AST 1828315.

This work made extensive use of the freely available Debian GNU/Linux operative system. We used the Python programming language (G. Rossum 1995), maintained and distributed by the Python Software Foundation. We made direct use of Python packages ASTROPY (Astropy Collaboration 2013, 2018), CORNER (D. Foreman-Mackey 2016), EMCEE (D. Foreman-Mackey et al. 2013), JWST (C. Alves de Oliveira et al. 2018), MATPLOTLIB (J. D. Hunter 2007), NUMPY (C. R. Harris et al. 2020), PROSPECTOR (B. D. Johnson et al. 2021) v2.0, PYNEB (V. Luridiana et al. 2015), PYTHON-FSPS (B. Johnson et al. 2023), PYSERSIC (I. Pasha & T. B. Miller 2023), QUBESPEC (J. Scholtz et al. 2025), and SCIPY (E. Jones et al. 2001). We also used the softwares FSPS (C. Conroy, J. E. Gunn & M. White 2009; C. Conroy & J. E. Gunn 2010), TOPCAT , (M. B. Taylor 2005), FITSMAP (R. Hausen & B. E. Robertson 2022), and DS9 (W. A. Joye & E. Mandel 2003).

DATA AVAILABILITY

This work is based on observations made with the NASA/ESA/CSA *James Webb Space Telescope*. Raw data were obtained from the Mikulski Archive for Space Telescopes at the Space Telescope Science Institute, which is operated by the Association of Universities for Research in Astronomy, Inc., under NASA contract NAS 5–03127 for *JWST*. These observations are associated with programme PID 3215. Reduced spectra and catalogues are available on the JADES website https://jades-survey.github.io/scientists/data.html and on the online database https://jades.herts.ac.uk/DR4/DarkHorse; for the data structure, please refer to the JADES DR4 (J. Scholtz et al. 2025). Supporting imaging and catalogues from PIDs 1210, 1286, 1287, 1895, 1963, 3215, and 6434 are available through the JADES DR5 (B. D. Johnson et al. 2026; B. E. Robertson et al. 2026). Supporting spectroscopic data from PID 1210 is available through the JADES public data release 1 (A. J. Bunker et al. 2024). Supporting spectroscopic data from PIDs 1180, 1181, 1286, 1287, and 3215 are available through the JADES public data relases 3 and 4 (J. Scholtz et al. 2025; F. D'Eugenio et al. 2025b).

REFERENCES

Alberts S. et al., 2024, ApJ, 975, 85

Alves de Oliveira C. et al., 2018, in Peck A. B., Seaman R. L., Benn C. R., eds, Proc. Conf Ser. Vol. 10704, Observatory Operations: Strategies, Processes, and Systems VII. SPIE, Bellingham, p. 107040Q

Asada Y. et al., 2025, ApJ, 983, L2
Asplund M., Grevesse N., Sauval A. J., Scott P., 2009, ARA&A, 47, 481
Astropy Collaboration, 2013, A&A, 558, A33
Astropy Collaboration, 2018, AJ, 156, 123
Baker W. M. et al., 2025, A&A, 697, A90
Baldwin J. A., Phillips M. M., Terlevich R., 1981, PASP, 93, 5
Belli S. et al., 2024, Nature, 630, 54
Bezanson R. et al., 2024, ApJ, 974, 92
Birkin J. E. et al., 2021, MNRAS, 501, 3926
Birkmann S. M. et al., 2022, in Coyle L. E., Matsuura S., Perrin M. D., eds, Proc. SPIE Conf. Ser. Vol. 12180, Space Telescopes and Instrumentation 2022: Optical, Infrared, and Millimeter Wave. SPIE, Bellingham, p. 121802P
Boyett K. et al., 2024, MNRAS, 535, 1796
Brammer G. B., van Dokkum P. G., Coppi P., 2008, ApJ, 686, 1503
Bunker A. J. et al., 2024, A&A, 690, A288
Capak P. L. et al., 2015, Nature, 522, 455
Carniani S. et al., 2017, A&A, 605, A42
Carniani S. et al., 2024, A&A, 685, A99
Cataldi E. et al., 2025, A&A, 703, A208
Ceverino D., Klessen R. S., Glover S. C. O., 2018, MNRAS, 480, 4842
Chabrier G., 2003, PASP, 115, 763
Charlot S., Fall S. M., 2000, ApJ, 539, 718
Conroy C., Gunn J. E., 2010, Astrophysics Source Code Library, record (ascl:1010.043)
Conroy C., Gunn J. E., White M., 2009, ApJ, 699, 486
Cooper R. A., Caputi K. I., Iani E., Rinaldi P., Desprez G., Navarro-Carrera R., 2025, ApJ, 994, 102
Covelo-Paz A. et al., 2026, A&A, 705, A155
Curti M. et al., 2023, MNRAS, 518, 425
Curti M. et al., 2024, A&A, 684, A75
Curtis-Lake E. et al., 2025, preprint (arXiv:2510.01033)
D'Eugenio F. et al., 2024, Nat. Astron., 8, 1443
D'Eugenio F. et al., 2025a, preprint (arXiv:2510.00101)
D'Eugenio F. et al., 2025b, ApJS, 277, 4
D'Eugenio F. et al., 2025c, MNRAS, 542, 960
D'Eugenio F. et al., 2026, MNRAS, 545, staf2117
Danhaive A. L. et al., 2025, MNRAS, 543, 3249
Davies R. L. et al., 2024, MNRAS, 528, 4976
Dome T., Tacchella S., Fialkov A., Ceverino D., Dekel A., Ginzburg O., Lapiner S., Looser T. J., 2024, MNRAS, 527, 2139
Dome T., Martin-Alvarez S., Tacchella S., Yuan Y., Sijacki D., 2025, MNRAS, 537, 629
Donnari M. et al., 2021a, MNRAS, 500, 4004
Donnari M., Pillepich A., Nelson D., Marinacci F., Vogelsberger M., Hernquist L., 2021b, MNRAS, 506, 4760
Eisenstein D. J. et al., 2025, ApJS, 281, 50
Eisenstein D. J. et al., 2026, ApJS, 283, 6
Endsley R., Stark D. P., Whitler L., Topping M. W., Chen Z., Plat A., Chisholm J., Charlot S., 2023, MNRAS, 524, 2312
Ferrara A., Pallottini A., Sommovigo L., 2025, A&A, 694, A286
Ferruit P. et al., 2022, A&A, 661, A81
Finkelstein S. L. et al., 2023, ApJ, 946, L13
Foreman-Mackey D., 2016, J. Open Source Softw., 1, 24
Foreman-Mackey D., Hogg D. W., Lang D., Goodman J., 2013, PASP, 125, 306
Fujimoto S. et al., 2023, ApJ, 949, L25
Gardner J. P. et al., 2023, PASP, 135, 068001
Gelli V., Salvadori S., Ferrara A., Pallottini A., 2024, ApJ, 964, 76
Gelli V., Pallottini A., Salvadori S., Ferrara A., Mason C., Carniani S., Ginolfi M., 2025, ApJ, 985, 126
Giardino G. et al., 2022, in Coyle L. E., Matsuura S., Perrin M. D., eds, Proc. SPIE Conf. Ser. Vol. 12180, Space Telescopes and Instrumentation 2022: Optical, Infrared, and Millimeter Wave. SPIE, Bellingham, p. 121800X
Gordon K. D., Clayton G. C., Misselt K. A., Landolt A. U., Wolff M. J., 2003, ApJ, 594, 279
de Graaff A. et al., 2025, A&A, 697, A189
Greene T. P. et al., 2017, J. Astron. Telesc. Instrum. Syst., 3, 035001
Hainline K. N. et al., 2024, ApJ, 964, 71
Harris C. R. et al., 2020, Nature, 585, 357
Hausen R., Robertson B. E., 2022, Astron. Comput., 39, 100586
Helton J. M. et al., 2024, ApJ, 974, 41
Hodge J. A. et al., 2013, ApJ, 768, 91
Hunter J. D., 2007, Comput. Sci. Eng., 9, 90
Inoue A. K. et al., 2016, Science, 352, 1559
Isobe Y., Ouchi M., Nakajima K., Harikane Y., Ono Y., Xu Y., Zhang Y., Umeda H., 2023, ApJ, 956, 139
Johnson B. et al., 2023, dfm/python-fsps: v0.4.4, Zenodo, https://doi.org/10.5281/zenodo.8230430
Johnson B. D., Leja J., Conroy C., Speagle J. S., 2021, ApJS, 254, 22
Johnson B. D. et al., 2026, preprint (arXiv:2601.15954)
Jones E. et al., 2001, SciPy: Open source scientific tools for Python, http://www.scipy.org/
Jones G. C. et al., 2025, MNRAS, 536, 2355
Joye W. A., Mandel E., 2003, in Payne H. E., Jedrzejewski R. I., Hook R. N., eds, ASP Conf. Ser. Vol. 295, Astronomical Data Analysis Software and Systems XII. Astron. Soc. Pac., San Francisco, p. 489
Juodžbalis I. et al., 2024, MNRAS, 535, 853
Karakla D., Shyrokov A., Pontoppidan K., Beck T., Gilbert K., Valenti J., Kassin S., Soderblom D., 2014, in Peck A. B., Benn C. R., Seaman R. L., eds, Proc. SPIE Conf. Ser. Vol. 9149, Observatory Operations: Strategies, Processes, and Systems V. SPIE, Bellingham, p. 91491Z
Kashino D., Lilly S. J., Matthee J., Eilers A.-C., Mackenzie R., Bordoloi R., Simcoe R. A., 2023, ApJ, 950, 66
Kennicutt R. C., Evans N. J., 2012, ARA&A, 50, 531
Kocevski D. D. et al., 2025, ApJ, 986, 126
Kriek M., Conroy C., 2013, ApJ, 775, L16
Kuruvanthodi A., Schaerer D., Marques-Chaves R., Korber D., Weibel A., Oesch P. A., Roberts-Borsani G., 2024, A&A, 691, A310
Laseter I. H. et al., 2024, A&A, 681, A70
Looser T. J. et al., 2024, Nature, 629, 53
Lovell C. C. et al., 2023, MNRAS, 525, 5520
Luridiana V., Morisset C., Shaw R. A., 2015, A&A, 573, A42
Madau P., Dickinson M., 2014, ARA&A, 52, 415
Maseda M. V. et al., 2024, A&A, 689, A73
Matthee J., Sobral D., Santos S., Röttgering H., Darvish B., Mobasher B., 2015, MNRAS, 451, 400
Matthee J. et al., 2024, ApJ, 963, 129
McClymont W. et al., 2025, MNRAS, 544, 513
Morishita T., Liu Z., Stiavelli M., Treu T., Bergamini P., Zhang Y., 2025, preprint (arXiv:2507.10521)
Nakajima K., Ouchi M., Isobe Y., Harikane Y., Zhang Y., Ono Y., Umeda H., Oguri M., 2023, ApJS, 269, 33
Nelson E. et al., 2024, ApJ, 976, L27
Noll S., Burgarella D., Giovannoli E., Buat V., Marcillac D., Muñoz-Mateos J. C., 2009, A&A, 507, 1793
Oesch P. et al., 2024, MNRAS, 525, 2864
Oke J. B., Gunn J. E., 1983, ApJ, 266, 713
Osterbrock D. E., Ferland G. J., 2006, Astrophysics of Gaseous Nebulae and Active Galactic Nuclei. University Science Books, Sausalito, California
Pasha I., Miller T. B., 2023, J. Open Source Softw., 8, 5703
Peng B. et al., 2025, A&A, 694, L1
Pérez-González P. G. et al., 2025, Nat. Astron., 9, 1240
Planck Collaboration VI, 2020, A&A, 641, A6
Rauscher B. J. et al., 2012, in Holland A. D., Beletic J. W., eds, Proc. SPIE Conf. Ser. Vol. 8453, High Energy, Optical, and Infrared Detectors for Astronomy V. SPIE, Bellingham, p. 84531F
Rieke M. J. et al., 2023, ApJS, 269, 16
Rigby J. et al., 2023, PASP, 135, 048001
Robertson B. E. et al., 2026, preprint (arXiv:2601.15956)
van Rossum G., 1995, CWI Technical Report, CS-R9526, Amsterdam
Rupke D. S., Veilleux S., Sanders D. B., 2005, ApJS, 160, 115
Rusakov V. et al., 2026, Nature, 649, 574
Sanders R. L. et al., 2025, preprint (arXiv:2508.10099)

Sandles L. et al., 2024, A&A, 691, A305
Scholtz J. et al., 2024, preprint (arXiv:2405.19401)
Scholtz J. et al., 2025, preprint (arXiv:2510.01034)
Shapley A. E., Sanders R. L., Reddy N. A., Topping M. W., Brammer G. B., 2023, ApJ, 954, 157
Simmonds C. et al., 2025, MNRAS, 544, 4551
Stark D. P. et al., 2015, MNRAS, 454, 1393
Strait V. et al., 2023, ApJ, 949, L23
Sun F. et al., 2025, preprint (arXiv:2503.15587)
Sun F. et al., 2026, preprint (arXiv:2601.15961)
Sun Y. et al., 2026, ApJ, 997, 140
Tacchella S., Bose S., Conroy C., Eisenstein D. J., Johnson B. D., 2018, ApJ, 868, 92
Tacchella S. et al., 2022, ApJ, 927, 170
Taylor E., Maltby D., Almaini O., Merrifield M., Wild V., Rowlands K., Harrold J., 2024, MNRAS, 535, 1684
Taylor M. B., 2005, in Shopbell P., Britton M., Ebert R., eds, ASP Conf. Ser. Vol. 347, Astronomical Data Analysis Software and Systems XIV. Astron. Soc. Pac., San Francisco, p. 29
Trussler J. A. A. et al., 2025, MNRAS, 537, 3662
Turner C. et al., 2025, MNRAS, 537, 1826
Valentino F. et al., 2025, A&A, 699, A358
Wang F. et al., 2023, ApJ, 951, L4
Williams C. C. et al., 2024, ApJ, 968, 34
Willott C. J. et al., 2022, PASP, 134, 025002
Witstok J. et al., 2025, Nature, 639, 897
Witstok J. et al., 2026, preprint (arXiv:2603.18775)
Woodrum C. et al., 2025, preprint (arXiv:2510.00235)
Wu P.-F., 2025, ApJ, 978, 131
Xu Y., Ouchi M., Nakajima K., Harikane Y., Isobe Y., Ono Y., Umeda H., Zhang Y., 2025, ApJ, 984, 182
Zhu Y. et al., 2025, ApJ, 986, 162
Ziparo F., Ferrara A., Sommovigo L., Kohandel M., 2023, MNRAS, 520, 2445

SUPPORTING INFORMATION

Supplementary data are available at *MNRAS* online.

suppl_data

Please note: Oxford University Press is not responsible for the content or functionality of any supporting materials supplied by the authors. Any queries (other than missing material) should be directed to the corresponding author for the article.

[1]*Kavli Institute for Cosmology, University of Cambridge, Madingley Road, Cambridge CB3 0HA, UK*
[2]*Cavendish Laboratory – Astrophysics Group, University of Cambridge, 19 JJ Thomson Avenue, Cambridge CB3 0HE, UK*
[3]*Department for Astrophysical and Planetary Science, University of Colorado, Boulder, CO 80309, USA*
[4]*Center for Astrophysics | Harvard & Smithsonian, 60 Garden St., Cambridge, MA 02138, USA*
[5]*Department of Physics and Astronomy, University College London, Gower Street, London WC1E 6BT, UK*
[6]*Scuola Normale Superiore, Piazza dei Cavalieri 7, I-56126 Pisa, Italy*
[7]*European Southern Observatory, Karl – Schwarzschild – Strasse 2, D-85748 Garching, Germany*
[8]*Steward Observatory, University of Arizona, 933 N. Cherry Ave., Tucson, AZ 85721, USA*
[9]*Department of Physics, University of Oxford, Denys Wilkinson Building, Keble Road, Oxford OX1 3RH, UK*
[10]*Department of Astronomy & Astrophysics, The Pennsylvania State University, University Park, PA 16802, USA*
[11]*Centro de Astrobiología (CAB), CSIC–INTA, Cra. de Ajalvir Km. 4, E-28850 Torrejón de Ardoz, Madrid, Spain*
[12]*Institut d'Astrophysique de Paris, Paris, 98 bis Boulevard Arago, F-75014 Paris, France*
[13]*Centre for Astrophysics Research, Department of Physics, Astronomy and Mathematics, University of Hertfordshire, Hatfield AL10 9AB, UK*
[14]*Department of Astronomy and Astrophysics, University of California, Santa Cruz, 1156 High Street, Santa Cruz, CA 96054, USA*
[15]*NSF National Optical-Infrared Astronomy Research Laboratory, 950 North Cherry Avenue, Tucson, AZ 85719, USA*
[16]*NRC Herzberg, 5071 West Saanich Rd, Victoria, BC V9E 2E7, Canada*
[17]*DARK, Niels Bohr Institute, University of Copenhagen, Jagtvej 155A, DK-2200 Copenhagen, Denmark*
[18]*AURA for European Space Agency, Space Telescope Science Institute, 3700 San Martin Drive. Baltimore, MD 21210, USA*
[19]*Instituto de Astrofísica, Pontificia Universidad Católica de Chile, Av. Vicuña Mackenna 4860, 782-0436 Macul, Santiago, Chile*
[20]*Max – Planck – Institut für extraterrestrische Physik (MPE), Gießenbachstraße 1, D-85748 Garching, Germany*
[21]*Cosmic Dawn Center (DAWN), Copenhagen, Denmark*
[22]*Niels Bohr Institute, University of Copenhagen, Jagtvej 128, DK-2200 Copenhagen, Denmark*

This paper has been typeset from a TEX/LATEX file prepared by the author.